CHAOS **18**, 026103 (2008)

# Twisted vortex filaments in the three-dimensional complex Ginzburg–Landau equation

Guillaume Rousseau,[1,a)] Hugues Chaté,[2,b)] and Raymond Kapral[3,c)]
[1]*INRIA Paris-Rocquencourt, Université Paris 7 Denis Diderot, Domaine de Voluceau, Rocquencourt—B.P. 105, 78153 Le Chesnay Cedex, France*
[2]*CEA—Service de Physique de l'Etat Condensé, Centre d'Etudes de Saclay, 91191 Gif-sur-Yvette, France*
[3]*Chemical Physics Theory Group, Department of Chemistry, University of Toronto, Toronto, Ontario M5S 3H6, Canada*

(Received 12 March 2008; accepted 20 May 2008; published online 27 June 2008)

The structure and dynamics of vortex filaments that form the cores of scroll waves in three-dimensional oscillatory media described by the complex Ginzburg–Landau equation are investigated. The study focuses on the role that twist plays in determining the bifurcation structure in various regions of the $(\alpha,\beta)$ parameter space of this equation. As the degree of twist increases, initially straight filaments first undergo a Hopf bifurcation to helical filaments; further increase in the twist leads to a secondary Hopf bifurcation that results in supercoiled helices. In addition, localized states composed of superhelical segments interspersed with helical segments are found. If the twist is zero, zigzag filaments are found in certain regions of the parameter space. In very large systems disordered states comprising zigzag and helical segments with positive and negative senses exist. The behavior of vortex filaments in different regions of the parameter space is explored in some detail. In particular, an instability for nonzero twist near the $\alpha=\beta$ line suggests the existence of a nonsaturating state that reduces the stability domain of straight filaments. The results are obtained through extensive simulations of the complex Ginzburg–Landau equation on large domains for long times, in conjunction with simulations on equivalent two-dimensional reductions of this equation and analytical considerations based on topological concepts. © *2008 American Institute of Physics*. [DOI: 10.1063/1.2940439]

**Scroll waves, the three-dimensional analogs of spiral waves, are one of the generic types of structures observed in oscillatory and excitable media. They are known to play important roles in the mechanisms that underlie cardiac fibrillation and have been observed and studied in experiments on chemical reacting systems. Just as spiral waves are organized around a core, scroll waves are organized around linelike filaments. Much of the scroll wave dynamics of a system can then be understood in terms the motions and bifurcations of these filaments. Due to the existence of inhomogeneities or boundary and initial conditions, these filaments may be twisted and the degree of twist can influence their structure, similar to the shapes a beam or telephone cord adopts when twisted. A detailed investigation of scroll wave filaments in oscillatory media is carried out to determine how their structure and dynamics changes as a function of the degree of twist they experience in various regions of parameter space. Filament structures, including straight, helical, zigzag, and complex disordered states, are found and characterized.**

## I. INTRODUCTION

Autonomous oscillations often occur in nonlinear chemical,[1] hydrodynamic,[2] and biological[3] extended systems. The complex Ginzburg–Landau equation (CGLE),

$$\partial_t A = A + (1+i\alpha)\nabla^2 A - (1+i\beta)|A|^2 A, \tag{1}$$

describes the slow modulations of the oscillations near a supercritical Hopf bifurcation in such media in terms of a complex amplitude $A$ and two real parameters, $\alpha$ and $\beta$.[2,4–6] This universal amplitude equation also qualitatively describes phenomena beyond the small-amplitude regime in the vicinity of the Hopf point.[7,8] In particular, some of the dynamical features of more complex oscillatory or excitable media are similar to those exhibited by the CGLE.[9,10]

In two space dimensions the zeros of $A$ are topological defects. Often they are sources of spiral waves and constitute organizing centers for the dynamics. In three space dimensions the points where $A$ vanishes generically form lines, or vortex filaments, which can be the centers of spiral scroll waves. The structure of the vortex filaments is determined by the topology of the phase field $\arg A$ and their dynamics follows from that of the full complex field $A$.

Results on the CGLE indicate that vortex filaments may have complicated structures or exhibit complex dynamics. For instance, untwisted vortex rings shrink and disappear in a large region of the $(\alpha,\beta)$ parameter space[11] and complex disordered states which arise from spontaneous stretching

---

[a)] Electronic mail: guillaume.rousseau@inria.fr.
[b)] Electronic mail: hugues.chate@cea.fr.
[c)] Electronic mail: rkapral@chem.utoronto.ca.

1054-1500/2008/18(2)/026103/21/$23.00

and bending of vortex filaments have been observed.[13,14] The linear stability of straight twisted and untwisted filaments has been determined.[15,16] Stable helical vortex filaments have been shown to arise from straight filaments by a Hopf bifurcation as the initial twist on the filament varies; further increase of the twist leads to a secondary Hopf bifurcation producing supercoiled vortex filaments.[16]

While the literature on the three-dimensional (3D) dynamics of vortex filaments in oscillatory media described by the CGLE is still relatively scarce, there are comparatively many corresponding studies in 3D excitable media.[17–21] Part of this interest stems from the role that the dynamics of vortex filaments may play in cardiac fibrillation.[22–25] Both simulations[26] and experiments[27] have shown that untwisted vortex rings slowly drift and shrink in some parameter domains. For other parameter values, such untwisted filaments and rings may expand.[26–40] Twisted vortex rings threaded by vortex filaments have also been studied numerically and exhibit similar complex behavior.[41,42] Twisted vortex filaments have been observed in experiments on the BZ reaction.[43] Stable helical vortex filaments have been found in studies of various reaction-diffusion models of excitable media.[17,18,44] Simulations have shown that if an initially straight vortex filament is given a certain amount of twist that exceeds a critical value, the filament will adopt a helical form with fixed radius.[45]

In this paper we investigate the structure of the vortex filament solutions of the CGLE. In particular, we show that one may observe a variety of filament types including helical and superhelical structures as well as more complex solutions comprising localized superhelical or zigzag pieces separated by helical segments. We discuss the bifurcations leading to these structures, varying the CGLE parameters and imposed twist.

The outline of the paper is as follows: After a discussion in Sec. II of some features of the CGLE and the topological properties of closed ribbon curves, Sec. III considers the stability of straight untwisted and twisted filaments to bifurcation to zigzag or helical structures. Full 3D simulations and a 2D projection of the 3D dynamics are used to investigate the bifurcation structure. Section IV describes more complex disordered regimes that are observed for large system sizes. The secondary bifurcation of the helical solution to supercoiled helical filaments is the topic of Sec. V, together with the emergence of localized superhelical structures. Section VI contains the concluding remarks. The appendices give the details of the numerical methods used in our simulations.

## II. PRELIMINARY CONSIDERATIONS

### A. Parameter space of the CGLE

The "phase diagram" of the CGLE in one and two space dimensions is rather well-known (Fig. 1).[46] Regions where spatiotemporal chaos occurs have been delimited and similar chaotic regimes are also observed in three dimensions. The family of plane-wave solutions of wave vector **k**,

$$A_{\mathbf{k}} = \sqrt{1-k^2}\exp[i(\omega_k t - \mathbf{k}\cdot\mathbf{x})], \tag{2}$$

with $\omega_k = -\beta + (\alpha-\beta)k^2$, exists in any space dimension and plays an important role in determining the structure of the $(\alpha,\beta)$ parameter space. These solutions are linearly unstable for $1+\alpha\beta<0$ (Benjamin–Feir limit).

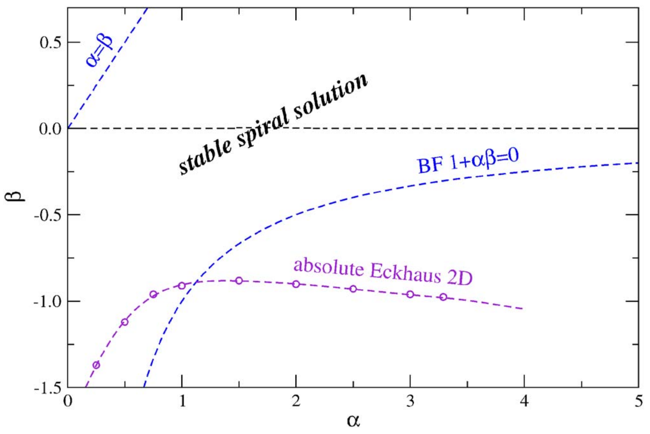

FIG. 1. (Color online) Parameter space of the 2D CGLE: the $\alpha=\beta$ line is the mirror symmetry line. Below the Benjamin–Feir line $1+\alpha\beta=0$ all plane wave solutions of the CGLE are linearly unstable. Below the Eckhaus line, the plane waves with the wavenumber of the spiral solution are absolutely unstable. The core instability line, denoting where the discrete modes of the spiral solution become linearly unstable, is at larger $\beta$ values out of the range covered in this figure.

In two space dimensions, the spiral solution with topological charge $\sigma=\pm 1$ plays a dominant role since solutions with higher topological charge are unstable.[47] Its general explicit form is not known but it can be written in polar coordinates $(r,\theta)$ as

$$A_s(r,\theta,t) = F(r)\exp i[\omega_s t - \sigma\theta + \psi(r)], \tag{3}$$

with $\omega_s = -\beta + (\beta-\alpha)k_s^2$, where $F(r)$ and $\psi(r)$ are two real functions whose asymptotic behavior for $r\to 0$ and $r\to\infty$ is $\lim_{r\to\infty} F(r) = \sqrt{1-k_s^2}$, $F(r)\propto r$ when $r\to 0$, and $\psi(r)\simeq k_s r$ when $r\to\infty$, $k_s$ is the asymptotic wave number of the spiral waves emitted by the core.[47] Many properties of this solution are known; for example, the limit of stability of the discrete core modes ("core instability line") has been determined.[12–14]

In the following study of the 3D case we restrict ourselves to the region of parameter space where the spiral solution is linearly stable, which implies stability of the core and at least absolute stability of the plane-wave of wave number $k_s(\alpha,\beta)$.[6]

### B. Vortex filaments as closed ribbon curves

In two space dimensions, pairs of opposite-charge vortices are involved in the creation and annihilation of topological defects, and the total topological charge must be zero in a finite system with periodic boundary conditions. The 3D case is more complicated. Assuming the topological charge of the spirals in planes transverse to any vortex filament is $\pm 1$, only closed vortex rings, including straight filaments, can be observed in a periodic box. The geometry of a vortex ring, like that of any closed curve, can be described by the rotations of the Frenet frame $(\mathbf{t},\mathbf{n},\mathbf{b})$ along the filament curve

$\mathbf{X}(s)$ parametrized by the arc length $s$. Here $\mathbf{t}$, $\mathbf{n}$, and $\mathbf{b}$ are, respectively, the tangent, normal, and binormal unit vectors. The structure of the filament may be characterized by the curvature $\kappa(s)=|d\mathbf{t}/ds|$ and the torsion $\tau(s)=|d\mathbf{b}/ds|$.

For the vortex filaments of the CGLE, one must also describe how the phase field is oriented with respect to the Frenet frame. Thus, the vortex filaments of oscillatory media are ribbons constructed from the filament curve $\mathbf{X}(s)$ and unit vectors $\mathbf{V}(s)$ giving the direction to specific but arbitrarily chosen values of the phase field at points normal to $\mathbf{t}(s)$ making an angle $\varphi$ with, say, the binormal $\mathbf{b}$.[48] White's theorem,[49]

$$\mathrm{Lk}=\mathrm{Tw}+\mathrm{Wr}=\mathrm{Tw}_f+\mathrm{Tw}_r+\mathrm{Wr}, \tag{4}$$

expresses the conservation law relating the (integer) link number Lk, which represents half of the sum of signed crossings of the two ribbon boundaries, to the sum of the twist Tw and writhe Wr of the ribbon. Here the twist $\mathrm{Tw}=\oint\tau(s)ds+\oint(d\varphi/ds)ds\equiv\mathrm{Tw}_f+\mathrm{Tw}_r$, may be decomposed into the twist of the filament $\mathrm{Tw}_f$ and the ribbon twist $\mathrm{Tw}_r$ which is the number of times the phase field is wrapped around the binormal along the curve. The writhe,

$$\mathrm{Wr}=\frac{1}{4\pi}\oint\oint\frac{[\mathbf{t}(t)\times\mathbf{t}(s)]\cdot[\mathbf{X}(t)-\mathbf{X}(s)]}{|\mathbf{X}(t)-\mathbf{X}(s)|^3}dtds, \tag{5}$$

quantifies the nonplanarity of the filament curve.

In the following, we will often consider infinite filaments with special symmetries such that the torsion and curvature are constant with $s$. This allows us to define densities of the topological quantities and to write a local version of White's theorem. In simulations, the 2D stable spiral solution is used to generate initial conditions with twist by shifting the phase of the spiral along the $z$ direction. The link density is a conserved quantity as long as no filament reconnection events occur.

### C. Single straight twisted filament

Consider a straight, infinite filament oriented along the $z$-axis, with a constant link per unit length $\gamma$. The solution of the three-dimensional CGLE for this case may be expressed in cylindrical coordinates $(r,\theta,z)$ as[16]

$$A_f=\sqrt{1-\gamma^2}F(r')\exp i[\omega_f t\pm(\theta+\gamma z)+\psi(r')], \tag{6}$$

where $r'=r\sqrt{1-\gamma^2}$ and $\omega_f=\omega_s(1-\gamma^2)-\gamma^2\alpha$, with $\omega_s$, $F$, and $\psi$ given by the 2D spiral solution (3). Below we shall study the stability of this solution.

In a finite box of height $L_z$ along $z$ which is periodic in $z$, as long as the filament is unbroken, the link number is conserved and $\gamma$ is quantized by the box size,

$$\mathrm{Lk}=2\pi n_t=\gamma L_z \quad (n_t\in\mathbb{Z}). \tag{7}$$

If the filament is straight, the Frenet frame is degenerate. The writhe is zero and one can choose to have $\mathrm{Tw}_f=0$ and $\mathrm{Lk}=\mathrm{Tw}_r$, so that $\gamma$ can also be seen as the (initial) phase twist density. The conservation of the total link requires one to consider $\gamma$ as an extra parameter of the problem in addition to $(\alpha,\beta)$, the usual parameters of the CGLE.

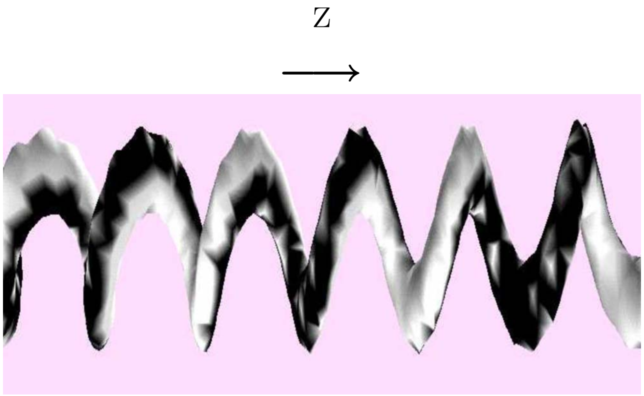

FIG. 2. (Color online) Stable helical vortex for $\alpha=1.7$, $\beta=0$, $\gamma=4\pi/128$, $L_z=640$ (the helical segment shown has length 200), $L_x=L_y=128$ and $dx=1$. A perspective view of the 3D isosurface $|A|=0.6$ colored by the phase field ($2\pi$-periodic gray scale) is displayed. Note that $\gamma_h\neq\gamma$ ($\gamma_h=42\pi/640$).

## III. FIRST INSTABILITY: HELICAL AND ZIGZAG SOLUTIONS

### A. 3D simulations and characterization of solutions

We first present the results of 3D simulations of the CGLE in a cylindrical box of height $L_z$, diameter $L_x=L_y$, periodic in $z$ with radial "outflow" boundary conditions in the horizontal plane. Radial outflow boundary conditions are discussed in Appendix A. We use a cubic lattice grid on which the Laplacian operator is expressed by second order finite differences. The time evolution is carried out using a simple, explicit, first-order Euler scheme. This simple scheme is most convenient given the large memory requirements of the 3D simulations. The position of the filament was determined by interpolation in all $(x,y)$ planes of the box, as discussed in Appendix B, since there is one defect per slice. Initial conditions were constructed by phase-twisting the 2D spiral solution for the same $(\alpha,\beta)$ values $n_t$ times along the $z$ axis.

Consider first the zero-link, $n_t=0$, case. For a large region of the $(\alpha,\beta)$ plane, the initial state quickly relaxes to solution (6), i.e., the system merely takes into account the amplitude, wavenumber, and frequency corrections with respect to the 2D spiral solution. However in other parameter regions the untwisted filament bifurcates to a zigzag filament[16] or to a disordered solution for large system sizes. This latter bifurcation will be discussed separately and in detail in Sec. IV.

Repeating this procedure for, say, $\alpha=1.7$ and $\beta=0$, and increasing the link per unit length $\gamma$, the straight filament remains stable up to some critical value $\gamma_c$. For larger $\gamma$ values, $\gamma=4\pi/128$ for instance, a helical vortex of pitch $\lambda_h\simeq 30$ is formed (Fig. 2), whose radius $R$ grows and saturates at a finite value $R\simeq 2.62$ (Fig. 3). Note that $\gamma_h\equiv 2\pi/\lambda_h\neq\gamma$. The radius of the helix is well defined since there is only one defect for a fixed $z$. Knowing the position $[x_f(z,t),y_f(z,t)]$ of the defect for each position $z$, the radius as a function of $z$, and $t$ is defined by

$$R(z,t)=\sqrt{(x_f-\langle x_f\rangle_z)^2+(y_f-\langle y_f\rangle_z)^2}. \tag{8}$$

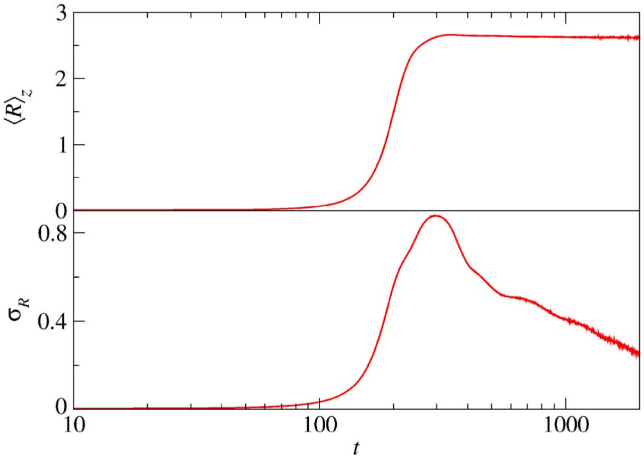

FIG. 3. (Color online) Simulation of the 3D CGLE for the same parameters as in Fig. 2. Growth of $\langle R\rangle_z$ the average radius along $z$ (upper curve) and its rms $\sigma_R$ (lower curve). Note that $\sigma_R$ tends to 0, signaling convergence to the same radius for all $z$ at late times.

The frequency of the asymptotic (far field) waves also changes from $\omega_f$ to $\omega_h$. The helix itself rotates with constant angular velocity $\omega$ and any point on it moves along the $z$-axis at a constant velocity $v=\omega/\gamma_h$. This velocity is just a phase velocity: a localized perturbation merely diffuses, i.e., the group velocity is zero. These results indicate that the straight filament has undergone a (supercritical) Hopf bifurcation to traveling waves. The direction of propagation and rotation is determined by the sign of $\gamma$, which breaks the $z\rightarrow -z$ parity symmetry.

The curvature and torsion of the helical solution are constant along the $z$-axis, $\kappa/(R\gamma_h)=\tau=\gamma_h/(1+R^2\gamma_h^2)$. We then have[44]

$$\frac{\mathrm{Tw}_f}{\mathrm{Lk}}=\frac{\gamma_h}{\gamma}-\frac{\mathrm{Wr}}{\mathrm{Lk}}=\frac{\gamma_h}{\gamma\sqrt{1+R^2\gamma_h^2}}, \tag{9}$$

and the ribbon twist is expressed as

$$\frac{\mathrm{Tw}_r}{\mathrm{Lk}}=1-\frac{\gamma_h}{\gamma}. \tag{10}$$

For the case $\alpha=1.7$, $\beta=0$, and $\gamma=4\pi/128$ reported above, this yields a *negative* ribbon twist which thus appears to "compensate" for the torsion arising from the instability.

The 3D calculations present a number of difficulties that hinder a detailed investigation of this bifurcation. As the bifurcation point is approached, the transient time diverges so that large-scale 3D simulations are especially lengthy. The finite system size and periodic boundary conditions along $z$ imply that only quantized values of the twist density can be investigated. In addition, again due to the finite system size, the system modes have a discrete set of wave vectors. The system geometry can influence the selected unstable wavevector and nonlinear coupling can lead to chaotic behavior which masks the true dynamics. For these reasons we have constructed a 2D projection of the 3D dynamics that allows us to explore the helix transition in detail.

## B. Equivalent 2D equation

In all the 3D simulations reported above, we observed that the helical symmetry,

$$A(r,\theta,z,t)=B(r,\phi=\theta-\gamma_h z,t)e^{i(\gamma-\sigma\gamma_h)z}, \tag{11}$$

was roughly preserved at all times, and certainly in the asymptotic state. (Note that time does not appear in the expression for the angular variable $\phi$ in agreement with the fact that the group velocity of the helix is zero.) Substitution into the CGLE yields[50]

$$\frac{\partial B}{\partial t}=(1-\gamma_p^2-i\alpha\gamma_p^2)B-(1+i\beta)|B|^2B+(1+i\alpha)\left(\nabla^2B+\gamma_h^2\frac{\partial^2B}{\partial\phi^2}+2i\gamma_h\gamma_p\frac{\partial B}{\partial\phi}\right), \tag{12}$$

where $\gamma_p=\gamma-\sigma\gamma_h$ can be interpreted as the phase twist density remaining after the helix has grown. In this 2D equivalent equation the pitch of the helix appears as an additional parameter, not determined by the instability mechanism.

Several observations can be made concerning the properties of the solutions of this equation in limiting cases. When $\gamma_h=0$, one has a twisted straight filament and Eq. (12) takes the form

$$\frac{\partial B}{\partial t}=(1-\gamma_p^2-i\alpha\gamma_p^2)B-(1+i\beta)|B|^2B+(1+i\alpha)\nabla^2B. \tag{13}$$

Under appropriate rescaling of space and time this equation reduces to the 2D CGLE with the same coefficients $\alpha$ and $\beta$. Consequently, for values of $\alpha$ and $\beta$ outside the core instability region, straight twisted solutions must have neutral stability and are delocalized since they correspond to a finite change of the solution at any space point. In the $\gamma=0$ case, the 2D equation is invariant under the change $\gamma_h\rightarrow-\gamma_h$ and the eigenvalue spectrum must be symmetric.

### *1. Numerical implementation of the 2D equivalent equation*

Equations like Eq. (12) are difficult to simulate; in particular, strong numerical instabilities arise from the term $\gamma_h^2(\partial^2B/\partial\phi^2)$. We have developed an integration method, detailed in Appendix C, that permits efficient simulation of Eq. (12) using a variable time step and a special spatial grid for circular domains.

The time evolution of the radius of the helix is shown in Fig. 4 for $\alpha=1.7$, $\beta=0$, $\gamma=4\pi/128$, $\gamma_h=8\pi/128$ using the 2D code with radial outflow boundary conditions. In this simulation, the initial condition was the (stable) spiral solution of the 2D CGLE at the same values of $\alpha$ and $\beta$. One first observes a short transient during which the instantaneous growth rate $\lambda(t)$ oscillates, reflecting the adjustment of the spiral wavelength, frequency, and amplitude to the 3D values. To remove this transient behavior, if necessary, it is possible to derive a 1D equivalent equation from Eq. (12) imposing the condition that the defect position is at $r=0$. This transient is followed by the rapid convergence of $\lambda(t)$ to its asymptotic constant value, permitting a very accurate measure of its magnitude and, thus, of the real part of the

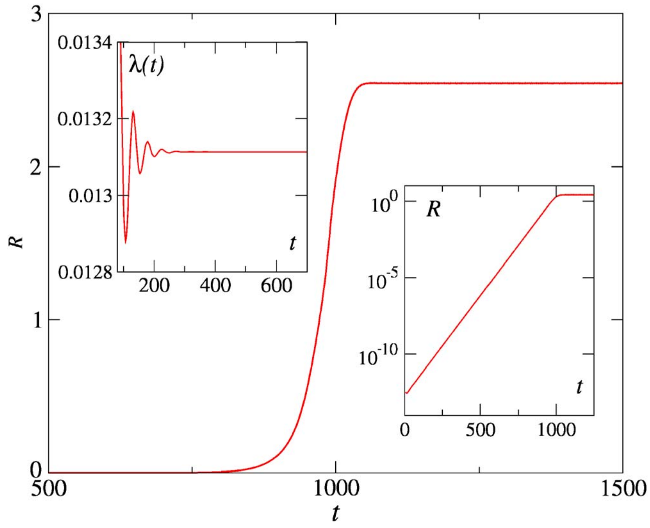

FIG. 4. (Color online) Simulation of the 2D equivalent equation (12). Radius $R(t)$ vs time for $\alpha=1.7$, $\beta=0$, $Lk=4\pi/128$, $\gamma_h=8\pi/128$ in a circular domain of radius $Nr=45$, radial step $dr=1$, with radial outflow boundary conditions. (Left inset) Oscillatory relaxation of the instantaneous growth rate $\lambda(t)$ during the early linear regime. (Right inset) Same as main graph in lin-log scales showing the exponential growth in the linear stage.

eigenvalue of the most unstable mode characterizing the linear instability. (Appendix C gives a more detailed comparison with 3D results.)

If initial conditions with spiral defect not located at (0,0) are used, an accurate estimate of negative eigenvalue of the less stable mode can be obtained.

### *2. Results for fixed $\alpha$, $\beta$, and $\gamma$*

We now use the equivalent 2D equation to investigate some detailed features of the helix bifurcations of the vortex filaments that are difficult to determine from full 3D simulations. In particular, we make use of the fact that $\gamma$ and $\gamma_h$ are now parameters and vary them continuously. This enables us to measure the most unstable (or least stable) eigenmode as a function of $\gamma_h$ at fixed $\gamma$.

For this purpose, we write the series expansion,

$$B(r,\theta,t)=\sum_{n=-\infty}^{+\infty} Z_n(r,t)e^{in\theta}. \tag{14}$$

In the linear regime, the $Z_n$ reduce to $[A_n(r)+iB_n(r)]e^{\Gamma_n t}$, where $\Gamma_n=\lambda_n+i\omega_n$ are the eigenvalues, the solutions of the linear problem. The $A_n$ and $B_n$ are easily obtained using Fourier decomposition,

$$Z_n(r,t)=\frac{1}{2\pi}\int_0^{2\pi} B(r,\theta,t)e^{-in\theta}d\theta. \tag{15}$$

The mode $n=\sigma$ is the reference solution [corresponding to the 3D solution (6)]. Our results show [Fig. 5(b)] that the most "dangerous" mode is always the $n=0$ mode, confirming the assumption made by Nam *et al.*[15] *A posteriori*, this is not surprising in the parameter region where the straight filament is unstable, since this mode is the only one leading to a displacement of the central filament.

We first focus on the parameter values $\alpha=1.7$ and $\beta=0$, and fix the link per unit length at $\gamma=4\pi/128$. Varying $\gamma_h$, we computed λ as well as the corresponding 2D eigenmode. The $\lambda(\gamma_h)$ data suggest the existence of two branches in the spectrum [Fig. 5(a)], a fact confirmed by the change in the structure of the eigenmode [Fig. 5(b)]. The central branch contains the neutral mode at $\gamma_h=0$ mentioned above. All modes in the central branch are *not* localized. The outer branch contains exponentially localized modes responsible for the instability of the solution. As $\gamma\to 0$, the spectrum becomes symmetric with respect to $\gamma_h=0$. (Further discussion of zigzag solutions and disordered states are given in Sec. IV.)

In the nonlinear stage, saturation occurs, as shown previously in Fig. 4. Varying $\gamma_h$, the maximum saturated radius does *not* appear at the value corresponding to the most unstable mode [compare Figs. 5(a) and 5(c)]. Nevertheless, both our 2D and 3D results indicate that the stable helix has a pitch corresponding to the most unstable linear mode. As

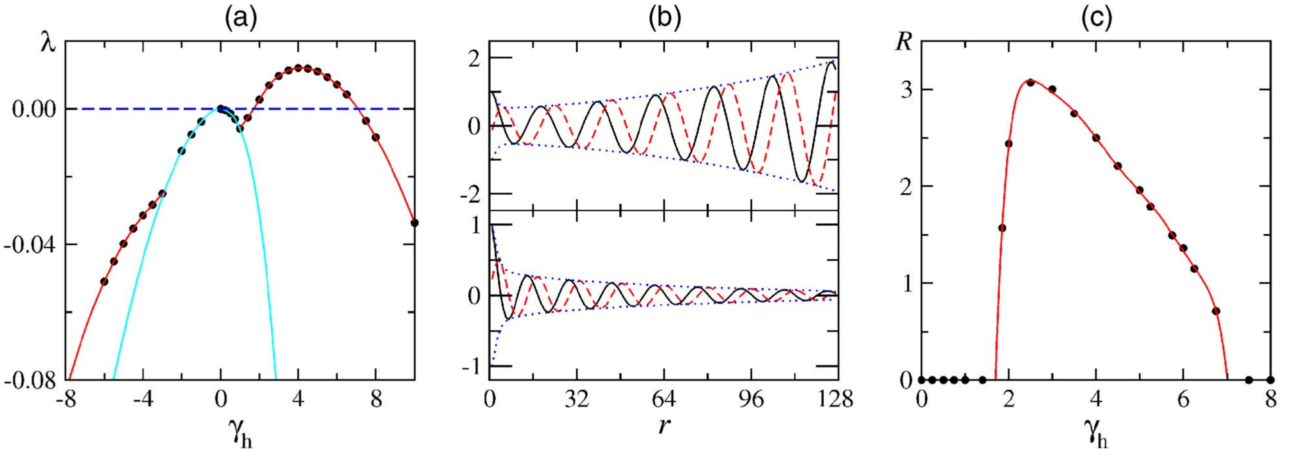

FIG. 5. (Color online) Stability analysis of the straight filament via the equivalent 2D equation ($\alpha=1.7$, $\beta=0$, $\gamma=4\pi/128$). (a) λ vs $\gamma_h$ (in units of $2\pi/128$). The lines are polynomial interpolations and should be regarded simply as guides to the eye. A detailed study of the associated modes [panel (b)] shows the existence of two separate branches. (b) Structure of the least stable or most unstable eigenmode for $\gamma_h=0.75$ (top) and $\gamma_h=1.4$ (bottom) (black solid lines: $A_0$; red dashed line: $B_0$; blue dotted lines: $\pm|Z_0|$). (c) Radius of the saturated helix vs $\gamma_h$ (in units of $2\pi/128$); the solid line is an eighth-order polynomial interpolation only intended as a guide to the eye.

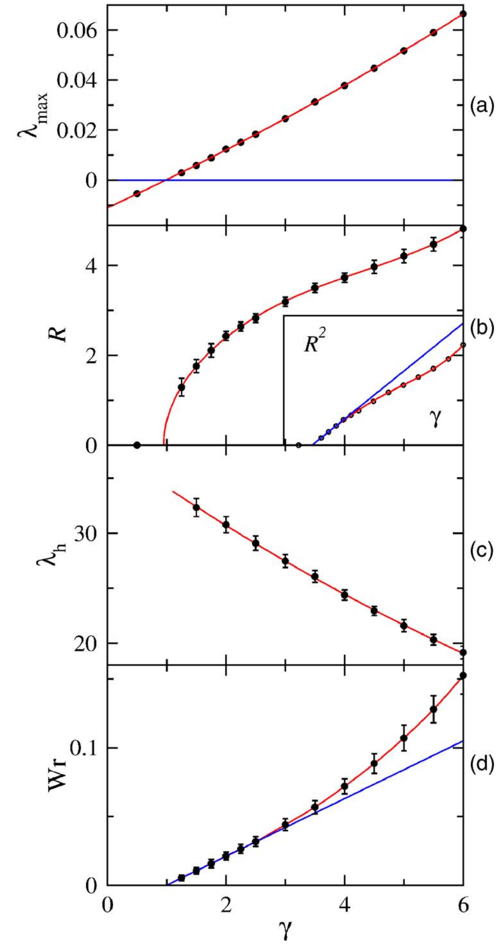

FIG. 6. (Color online) Linear stability and nonlinear fate of the straight filament as a function of $\gamma$ (in units of $2\pi/128$) for $\alpha=1.7$, $\beta=0$, using the 2D equivalent equation. (a) Real part of the eigenvalue. The threshold is approximately the same as that obtained using the radius [panel (b)]. (b) Radius and square radius (inset) of the saturated helix. (c) Pitch of the helix. (d) Writhe of the helix.

the threshold is approached, one observes that the difference between the two radius values decreases.

We now study in detail the instability of the straight filament as the link per unit length $\gamma$ increases. Keeping $\alpha=1.7$ and $\beta=0$ fixed, we observe that the filament becomes unstable at $\gamma_c \simeq 1.12\pi/128$. The maximum growth rate $\lambda_{max}$ varies smoothly with $\gamma$ across the threshold and in the entire range of $\gamma$ values we have investigated [Fig. 6(a)]. This allows a precise estimation of the position of the threshold and is less sensitive to numerical problems close to the threshold. The saturated radius shows the expected behavior near a supercritical Hopf bifurcation, $R^2 \sim (\gamma-\gamma_c)$ [Fig. 6(b)].

We observe that the pitch $\lambda_h$ decreases with increasing $\gamma > \gamma_c$ [Fig. 6(c)], and thus the magnitude of $\mathrm{Tw}_r$ increases. Finally, the writhe of the helix [Fig. 6(d)] is observed to vary linearly with $\gamma$ in the vicinity of $\gamma_c$. Using Eq. (9), this property is expected as long as $R^2 \propto (\gamma-\gamma_c)$ and $\lim_{\gamma\to\gamma_c}\gamma_h=\gamma_h^c \neq 0$. As already mentioned in Ref. 16, the conversion of a constant proportion of the excess twist into writhe is akin to the behavior of elastic rods (see Refs. 48 and 51, and references therein).

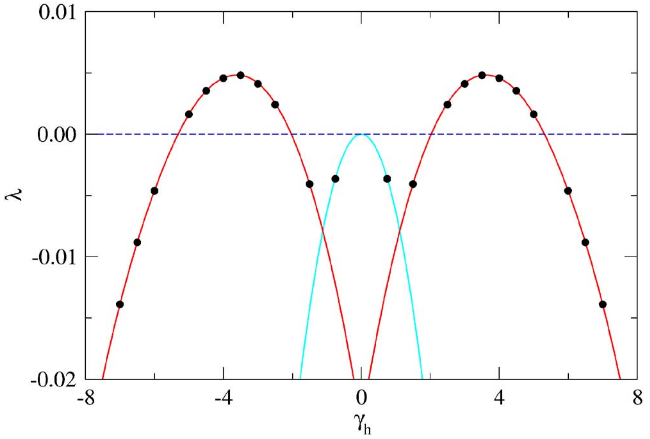

FIG. 7. (Color online) Same as Fig. 5(a) but for $\alpha=2.25$, $\beta=0$, $\gamma=0$. The lines are polynomial interpolations and should be regarded simply as guides to the eye. A detailed study of the corresponding modes shows the existence of two separate branches. Notice the symmetry of the eigenspectrum with respect to $\gamma_h=0$.

### C. Linear stability region in parameter space

We now discuss the extent to which the results presented above for $\alpha=1.7$ and $\beta=0$ are representative of other parameter values.

The untwisted ($\gamma=0$) filament solution has a special status: it does not break the $z\to -z$ parity symmetry. Accordingly, the spectrum is then symmetric (Fig. 7). As shown below, this has consequences in the nonlinear stage of its instability. The $\gamma_c(\alpha,\beta)=0$ curve was first determined by Aranson *et al.*[12] using a reduced linear stability analysis similar to that employed by Nam *et al.*[15] These two studies and our partial results presented in Ref. 16 are in accord. The $\gamma_c=0$ line lies well within the 2D spiral core stability region (Fig. 9 in Ref. 14 and Fig. 2 in Ref. 15): the 3D untwisted filament solution is less stable than the 2D spiral solution.

For fixed values of $\gamma$, Nam *et al.*[15] determined the locations of the curves $\gamma_c(\alpha,\beta)=\mathrm{Cst}$ marking the stability limits of solution (6). As discussed in Refs. 15 and 16, this limit defines a large area, removed from the core instability region and the absolute instability limit of the plane waves emitted by the 2D spiral solution, in which straight filaments are unstable.

For nonzero values of the link density, the symmetry of the eigenspectrum is broken. A new situation may occur when only a single branch of the spectrum is unstable. Only one unstable mode is enough to produce an instability of a straight filament, but the existence of two families of unstable modes will influence the nature of the dynamical regimes observed (this is discussed in Sec. IV). Figure 8 shows symmetry breaking and the existence of two different instability regions, depending of the number of unstable branches. When the link density increases, the size of the intermediate region also increases.

An instability region lying close to the $\alpha=\beta$ line was reported in Ref. 15. This region does not exist for $\gamma=0$. For values of the link density considered by Nam *et al.*,[15] this region reconnects with the instability region described previously for larger values of $\alpha$. Using the 2D equivalent equa-

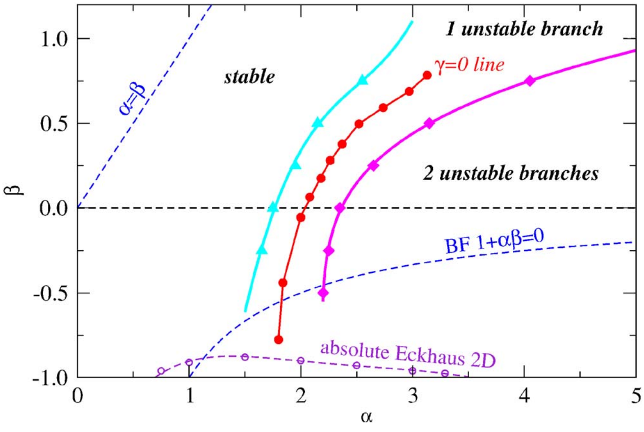

FIG. 8. (Color online) Systematic study, via the 2D equivalent equation, of the linear stability of the filament solution for $\gamma=1$ $(2\pi/128)$. The straight filament is stable to the left of the thick cyan line (triangles). Between this line and the thick magenta line (diamonds), there is one unstable branch in the spectrum (with pitch of the same sign as the link density). To the right of the magenta line, there are two unstable branches in the spectrum. The red solid line (circles) in the middle is the instability limit for $\gamma=0$ from Ref. 15, which is in agreement with our results.

tion, we carried out a study in the linear stage of the evolution (Fig. 9). This new region is of particular interest, because the asymptotic wave number of the spiral vanishes along the $\alpha=\beta$ symmetry line and interactions become long range.[6] Also, the nature of the instability in the nonlinear stage of the evolution is different and does not lead to a stable helical filament (see next section).

The instability region was studied carefully using large simulation domains and long integration times. In addition, we attempted to determine whether the region always exists for nonzero values of the link density, and if the reconnection between the two (sub-)regions of instability always exists. In carrying out this study, a new numerical difficulty was encountered, since we observed that $\gamma_h^c \to 0$ when $|\alpha-\beta| \to 0$. Because of the finite size of the spiral core and of the increasing wavelength of the emitted waves, it was very difficult to obtain an accurate numerical estimate of $\gamma_h^c$. We were not able to obtain definitive answers to the above questions and they remain as open problems for further study. The use of a modified version of our 2D program using a variable grid size in the radial direction could prove useful in this connection.

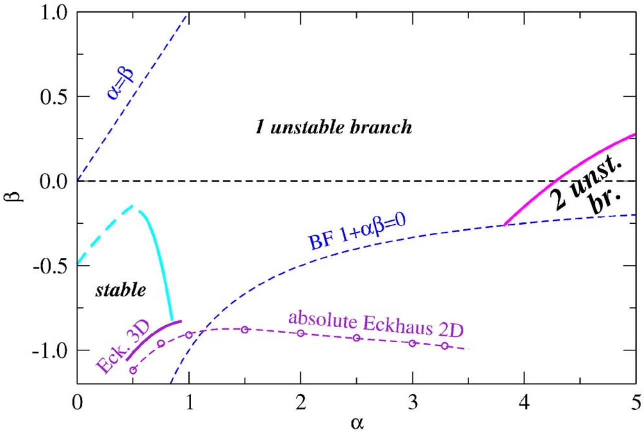

FIG. 9. (Color online) Same as Fig. 8, but for $\gamma=4$ $(2\pi/128)$. The stability is reduced to the left region between the two thick cyan lines and the absolute instability limit of the emitted waves (Eckhaus 3D), which is shifted relative to its location for $\gamma=0$, in agreement with Ref. 15.

## D. Nonlinear stage

### 1. Bounded versus unbounded growth for $\gamma \neq 0$

Nam *et al.*[15] did not draw any conclusions about the saturation of the helical solution in the instability region for low values of $\alpha$. They observed saturation but suspected that boundary effects associated with the small size of their simulation box could play a role. We investigated this point in both the linear and nonlinear stages of the evolution.

In the nonlinear stage, our simulation of the 2D equation (12) did not show saturation of the instability in the region around the $\alpha=\beta$ line, in contradiction with the 3D simulations they report. Our simulation of the 3D CGLE in a periodic box of size comparable to that used in Ref. 15 did yield a saturated solution, but using larger simulation boxes and/or outflow boundary conditions we found that saturation does not occur, or is due to interactions with mirror filaments in the case of periodic boundary conditions.

The simulation of the 2D equivalent equation allows one to study the linear and nonlinear stages of the evolution of the helical solution growing in very large domains. We have determined the most unstable mode for the case shown in Ref. 15 [Fig. 4(b)], namely, $\alpha=0.3$, $\beta=-0.2$, $\gamma=4$ $(2\pi/128) \simeq 0.196$ in our notation. We find that the pitch of the most unstable helix is about 2.41 $(2\pi/128)$. Figure 10(a) shows the radius versus time starting from a straight filament. One can see that there is no sign of saturation until the defect is close to the boundary, where growth is arrested and the defect rotates along the disk perimeter. Figure 11 shows the corresponding phase and amplitude fields at different times. One can remark that in the third and fourth panels the wavelength becomes very large. This corresponds to the time where the rotation of the defect changes sign. We have checked that the point where this occurs is not dependent of the system size. Note that $\gamma_h < \gamma$ in this region, which implies that $\mathrm{Tw}_r > 0$. However there are other cases where $\mathrm{Tw}_r > 0$ and a saturated helix is observed [Fig. 10(b)]. These results confirm the existence of a significant change in the nonlinear regime of this instability for small values of $\alpha$, even if its origin is still unresolved.

We performed a systematic study of the problem using the 2D equivalent equation, scanning the $(\alpha,\beta)$ parameter space, keeping $\gamma$ constant and varying $\gamma_h$. "Unbounded growth" was concluded when at least one value of $\gamma_h$ led to a radius of more than half the simulation domain radius. This criterion could be improved, by first localizing the most unstable mode, and then checking if it leads to saturation or not. In addition, full 3D simulations must be performed to extend 2D simulation results to the 3D equation.

Figure 12 summarizes the results of our 2D study. It shows the existence of a very large domain of unbounded growth. Since this unsaturated region corresponds to the left part of the unstable region, it confirms that the instability region previously described is probably the result of the re-

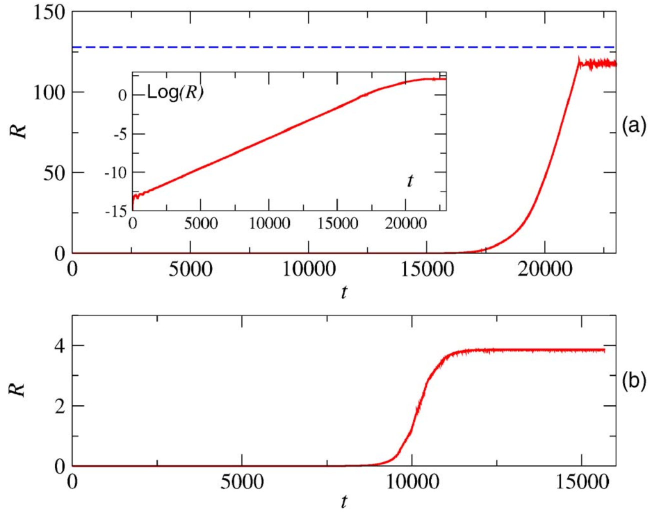

FIG. 10. (Color online) Unbounded and bounded growth in simulations of the 2D equivalent equation. (a) Radius $R$ and $\log R$ (inset) vs time $t$ for $\alpha=0.3$, $\beta=-0.2$, $\gamma=4\ (2\pi/128)$, $\gamma_h=2.4\ (2\pi/128)$. This pitch is close to the most unstable mode. The horizontal dashed line corresponds to the boundary limit (circular domain of radius 128). (b) Same as (a) but for $\alpha=0.5$, $\beta=-0.1$, $\gamma=4\ (2\pi/128)$, $\gamma_h=3\ (2\pi/128)$. This pitch is also close to the most unstable mode. One observes the saturation of the instability although $\mathrm{Tw}_r>0$.

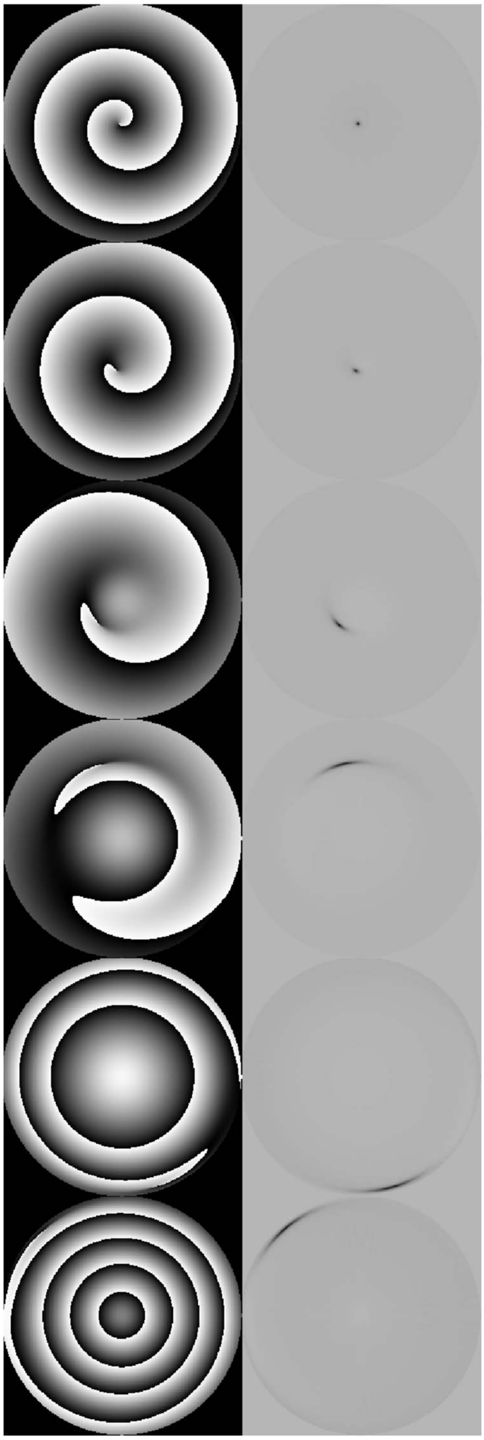

FIG. 11. Amplitude field (right) and phase field (left) at times $t=17\,000, 18\,000, 19\,000, 20\,000, 21\,000, 22\,000$ (from top to bottom) during the same run as in Fig. 10(a) ($\alpha=0.3$, $\beta=-0.2$, $\gamma=42\pi/128$, $\gamma_h=2.42\pi/128$). The rotation of the core changes sign around $t=20\,000$.

connection of two different regions of instability. Further studies will have to be carried out to improve our understanding of the nature of these instabilities in both the linear and the nonlinear stages of the evolution. In particular, the reconnection of the regions should be investigated for small values of the link density. These issues are difficult to resolve using numerical simulations and will require variable radial grid size algorithms and long simulation times.

### 2. Zigzag solutions for $\gamma=0$ in small systems

When $\gamma=0$, symmetry arguments ($z\to -z$ parity) demand that $+z$- and $-z$-going traveling waves arise from the instability (symmetry of the eigenspectrum with respect to $\gamma_h=0$ in Fig. 7). Generically, in the nonlinear stage, one expects either one set of traveling waves to eventually dominate, or a standing wave pattern to form in which the two corresponding amplitudes are equal. This usually depends on the effective nonlinear coupling coefficient between the two coupled 1D CGLE acting as amplitude equations in the vicinity of threshold.[52,53]

In Ref. 16, using 3D simulations with system sizes in the $z$ direction of about 10–20 $\lambda_h$ of the most unstable helix in the linear stage of the evolution, we showed, for $\gamma=0$, that the instability saturates and leads to "zigzag" patterns (Fig. 13 in Ref. 16). These $z$-periodic structures with wavelength $\lambda_{zz}$ are flat, and rotate uniformly about the $z$-axis with a frequency $\omega_{zz}$. Although we have not explored the vicinity of the $\gamma_c=0$ line completely, all of our results with similar domain sizes show zigzag filaments and not helices. This is in contradiction with the results of 3D simulations presented by Aranson *et al.*,[14] who show a regular helical filament arising from the instability. This may be due to their use of special perturbations of the solution (3) which break the $z\to -z$ symmetry. The Hopf bifurcation with $\gamma=0$ is an O(2) Hopf bifurcation and standing wave solutions must respect this spatial reflection symmetry.[54]

It is easy to show that the zigzag filaments are the analogs of standing waves, i.e., they correspond to the superposition of two helices. Consider the superposition of two helices of opposite pitch $\pm\gamma_h$, same radius $R_h$, and same angular velocity $\omega$, parametrized by $(x_\pm, y_\pm, z)$ according to

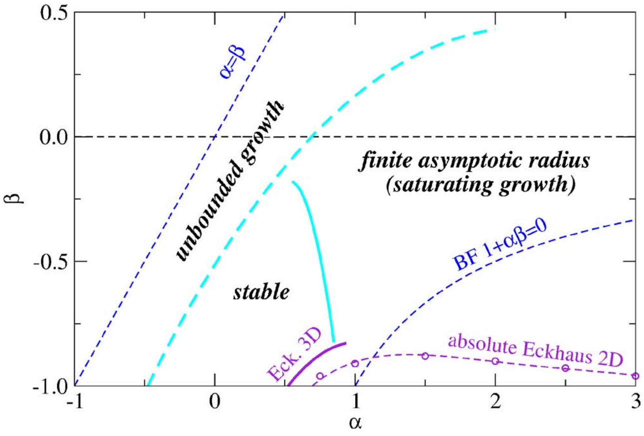

FIG. 12. (Color online) Same as Fig. 9, but at the nonlinear stage. The thick dashed cyan line which closes the stability region now extends to larger $\alpha$ and $\beta$ values. It separates unbounded growth [as in Figs. 10(a) and 11] from finite asymptotic radius helices.

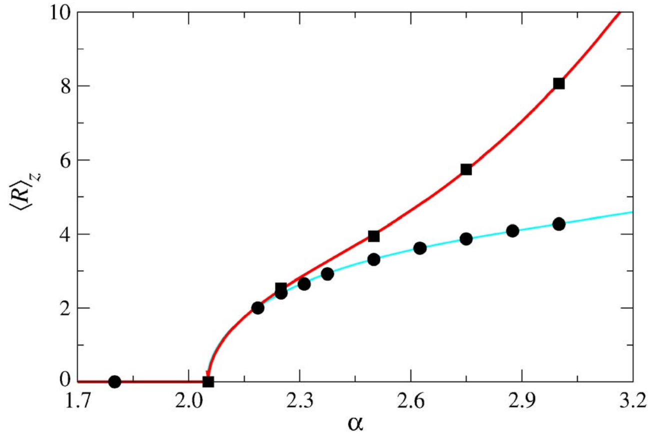

FIG. 14. (Color online) $\langle R\rangle_z$ vs $\alpha$ for $\beta=0$, $\gamma=0$. The square symbols correspond to 3D simulation results for $L_x=128$, $L_y=128$, $L_z$ between 256 and 512, and $dx=1$. The circles correspond to the linear superposition of the 2D solutions (valid close to the threshold, $\alpha_c \simeq 2.05$).

$$(x^{\pm},y^{\pm}) = R_h e^{i\phi^{\pm}(z,t)} = R_h e^{i(\omega t \pm \gamma_h z + \phi_0^{\pm})}. \tag{16}$$

In the linear stage of the instability (near threshold), one expects to observe the superposition of these two helical modes:

$$(x_{zz},y_{zz}) = 2R_h \cos\left(\gamma_h z + \frac{\phi_0^+ - \phi_0^-}{2}\right) \times \exp\left(i\omega t + i\frac{\phi_0^+ + \phi_0^-}{2}\right), \tag{17}$$

which describes a flat zigzag filament of wavelength $\lambda_{zz} = \lambda_h$, maximum radius $R_{\max}=2R_h$, rotating about the $z$-axis with frequency $\omega_{zz}=\omega$. One can further calculate that, near threshold, the $z$-averaged radius of a zigzag filament should be $2R_{\max}/\pi$.

Moving away from the threshold, one observes the expected behavior for the amplitude near a Hopf bifurcation, i.e., $\langle R^2\rangle \sim (\alpha-\alpha_c)$. Figure 14 shows the average radius along $z$, $\langle R\rangle_z$, versus $\alpha$, along with the expected value assuming superposition of the saturated helical modes, $4R_h/\pi$. As expected, far from the threshold this hypothesis is no longer true, indicating that nonlinear effects come into play and the solution is no longer a superposition of two independent helical modes.

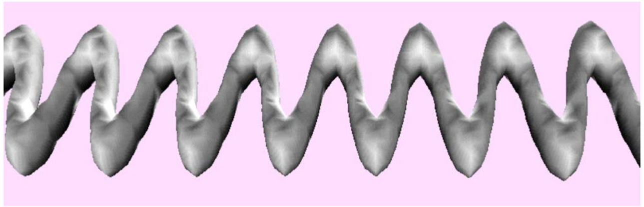

FIG. 13. (Color online) 3D isosurface colored by the phase field showing a flat zigzag asymptotic solution for $\alpha=2.5$ and $\beta=0$.

## IV. DISORDERED STATES IN LARGE SYSTEMS

The previous results show that when only one branch is unstable in the spectrum, one observes either stable finite-radius "helices" or unbounded growth of some helical mode (using the 2D equivalent equation). In 3D, the stable helices can be observed in arbitrarily long domains. When two branches are unstable the 2D equation shows finite-radius "helices." In this section we show that, however, 3D simulations in long domains lead to spatiotemporally disordered states at the nonlinear level. This is true even for $\gamma=0$ when the two branches become unstable simultaneously: the zigzag solutions described above in small systems are actually unstable in larger domains (see below).

We now describe these disordered states by reporting in detail our observations on two long simulation runs performed on very large domains, one for $\gamma=0$ and another at a nonzero value of $\gamma$.

### A. $\gamma=0$

When $\gamma=0$ the two branches of the spectrum become unstable simultaneously. For small systems, as reported above, stable zigzag solutions are observed in small systems. But significantly increasing the system size up to more than 100 wavelengths of the most unstable helix, one observes disordered states.

Figure 15 shows the final filament after an integration time $\Delta t=30\,000$ for $\alpha=2.25$, $\beta=0$, and a system size 4096 $\simeq 120\lambda_h$ in the $z$-direction. One can distinguish at least 4 or 5 regions inside which simple helical or zigzag solutions are observed (Fig. 16). The helical solutions can be further distinguished by the sign of their local twist density and of their local pitch. Thus, the region from $z\simeq 3400$ to $z\simeq 800$ (boundary conditions are periodic in $z$), is labeled "helix$^{++}$" in Fig. 16 because both its twist density and its pitch are

FIG. 15. Simple perspective plot of the 3D filament curve obtained for $\alpha=2.25$, $\beta=0$, $\gamma=0$, $L_x \times L_y \times L_z = 128 \times 128 \times 4096$, $t=30\,000$. In this disordered state, different regions can be distinguished (see text).

positive. Similarly, the second helical region (from $z \simeq 1050$ to $z \simeq 2000$, is labeled "helix$^{--}$" because both quantities are negative.

Such (local) topological quantities are useful to describe the various local states, since they are related to the globally conserved quantities that enter as new parameters of the system imposed by the initial conditions. Figure 16(c) shows the local link density along the filament of Fig. 15. There are large fluctuations in the zigzag regions associated with the discontinuity of quantities like the filament phase. Even if the integral over $z$ is equal to 0, the local link density is nonzero almost everywhere; in this regime, the global symmetry is broken locally. Figure 16 also shows that the pitch of the helix does not always have the same sign as the local link density. The selection mechanism for the value of the local link density, $\sim \pm 0.25$ $(2\pi/128)$, is unresolved and may be influenced by finite size effects. We expect that increasing the system size further will allow stronger symmetry breaking and larger values of the local link density.

Next, we study this regime from the spatiotemporal point of view. In Fig. 17, which shows spatiotemporal plots of $\langle d\phi/dz(z,t)\rangle_{\Delta z}$ and $\sigma_{\Delta_z}(d\phi/dz)$, symmetry breaking is obvious. The pattern obtained by inverting "black" and "white"

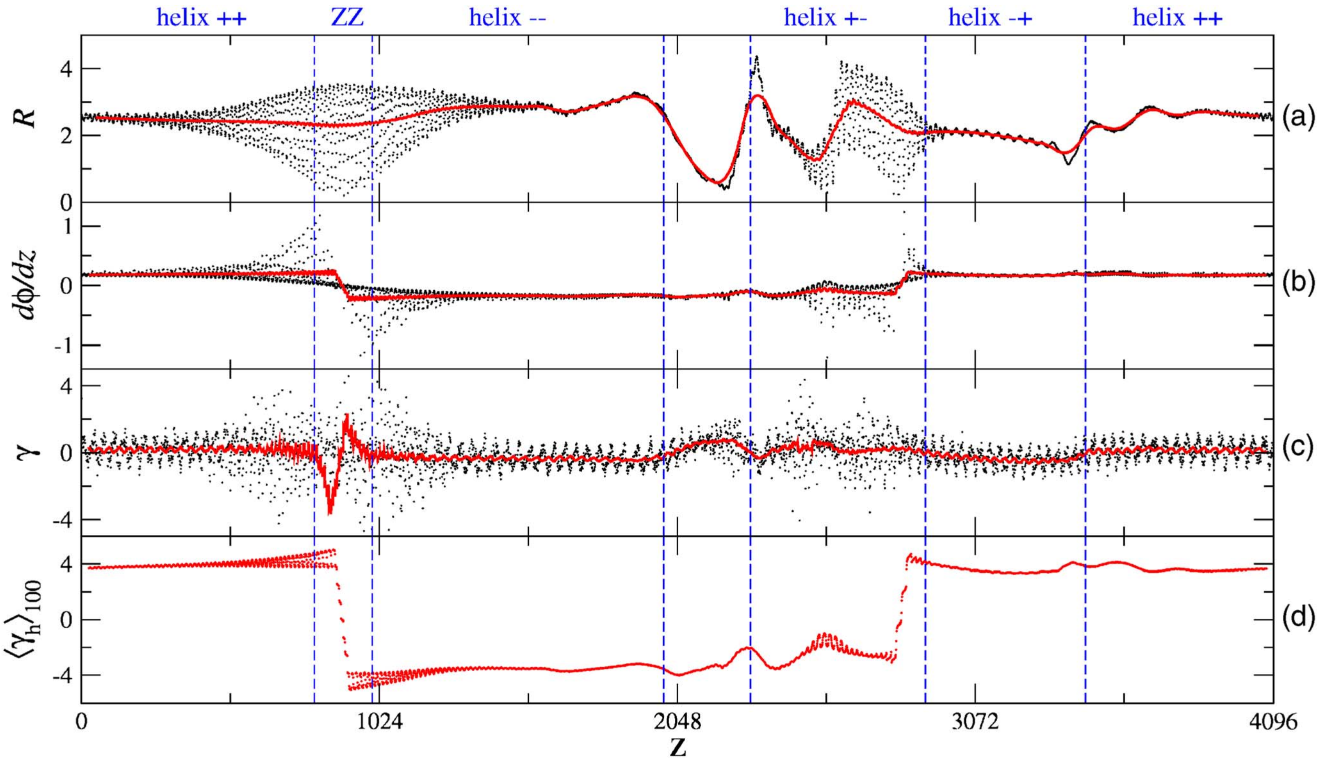

FIG. 16. (Color online) Detailed analysis of the filament curve shown in Fig. 15. From top to bottom: (a) radius $R(z)$ (black dots) and locally averaged radius $\langle R(z)\rangle_{\Delta z}$ (red solid line, $\Delta z=100$). (b) Same as (a) but for phase gradient $d\phi/dz$. The filament is roughly composed of two different regions where the filament rotates in opposite directions. Regions of large fluctuations are associated with flat helices or twisted zigzag solutions. (c) Same as (a) and (b) but for the local link density along the filament. Note the large fluctuation in the zigzag region associated with the discontinuity in quantities like the filament phase. The local link density is almost nonzero everywhere even if the total link is zero. (d) Local average of the local pitch $\langle \gamma_h = d\phi/dz\rangle_{\Delta z}$. Note that the observed pitch $\sim 4$ $(2\pi/128)$ corresponds to the most unstable mode in Fig. 7.

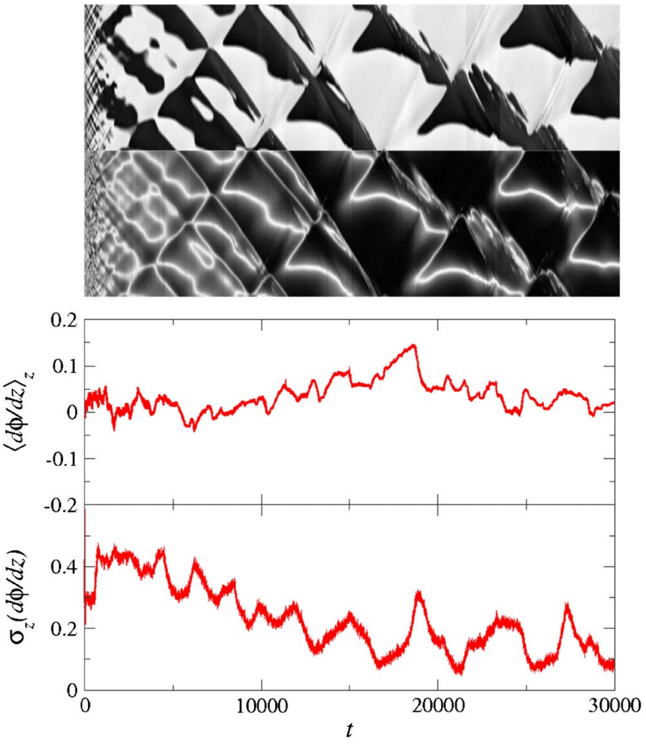

FIG. 17. (Color online) Time-evolution of various quantities during the run leading to the solution shown in Fig. 15. (Top two panels) Spatiotemporal diagrams (time is running from left to right) showing $\langle d\phi/dz(z,t)\rangle_{\Delta z}$ and $\sigma_{\Delta_z}(d\phi/dz)$. (Bottom two time-series) Average and rms of these quantities as a function of time. Parameters: $\alpha=2.25$, $\beta=0$, $\gamma=0$, $\Delta z=100$, $t\in[1-30000]$, $z\in[1:4096]$. A linear gray scale is used between instantaneous min (black) and max (white) values.

regions is not the same. Moreover, the temporal evolution of the average value of $d\phi/dz$ oscillates between 0 and 0.2, which is the pitch of the most unstable mode. This leads us to predict that two disordered states may exist after symmetry breaking in the nonlinear stage of the evolution. However, the system is clearly too small, since we observe only two regions coexisting in $z$. Simulations should be performed with larger system sizes and longer integration times to draw firm conclusions about these system states.

Figure 18 shows the spatiotemporal evolution for the locally averaged radius, its rms and the temporal evolution of the average values of these quantities over the system size. The zeros of the radius are indeed splitting points for left and right propagating waves. This pattern resembles some 1D spatiotemporal intermittency regimes with coexisting plane waves and holes viewed as local structures.[8,46] In our case, "plane waves" correspond to families of helical solutions, and a hole corresponds to a localized depression of the radius (as, for instance, at $t=30000$ around $z\sim2250$ in Fig. 16). This picture of the dynamics is also suggested by the temporal evolution of the radius at a given position in $z=z_0$ (bottom panel), where the average value is defined, but large variations are observed locally. Again the system is too small to draw definitive conclusions about the existence of a spatiotemporal intermittency regime.

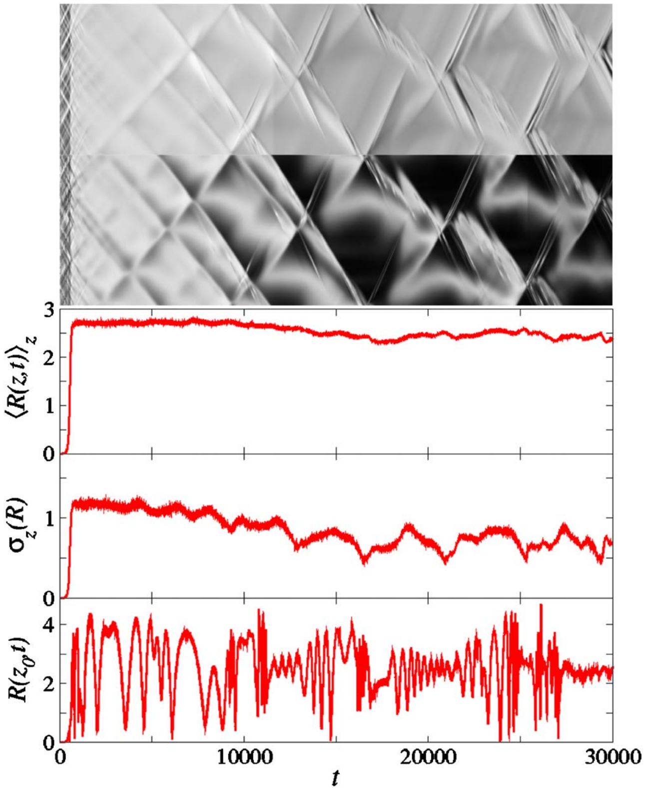

FIG. 18. (Color online) Same as Fig. 17, but for quantities related to the radius of the filament. From top to bottom: $\langle R(z,t)\rangle_{\Delta z}$, $\sigma_{\Delta z}(R)$, $\langle R(z,t)\rangle_z$, $\sigma_z(R)$, and $R(z_0,t)$.

## B. $\gamma\neq0$

For $\alpha=2.25$, $\beta=0$, and $\gamma=-1/8$ $(2\pi/128)$ both branches of the spectrum are unstable but the growth rates are not symmetric. Starting from a straight filament, one already observes symmetry breaking during the linear stage of the evolution as can be seen in Fig. 19. Figure 20 plots the filament curve after a run similar to that in Fig. 15, and Fig. 21 plots local quantities like those in Fig. 16. We can see, as observed for the $\gamma=0$ case, the coexistence of different local solutions.

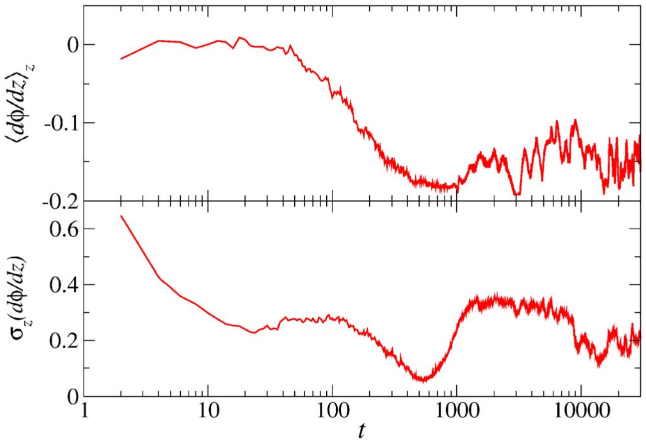

FIG. 19. (Color online) Time series of $\langle d\phi/dz\rangle_z$ (top) and $\sigma_z(d\phi/dz)$ (bottom) for $\alpha=2.25$, $\beta=0$, and $\gamma=-1/8$ $(2\pi/128)$. 3D simulation in a domain of size $L_x\times L_y\times L_z=128\times128\times4096$ (see following figures). Symmetry-breaking occurs during the linear stage.

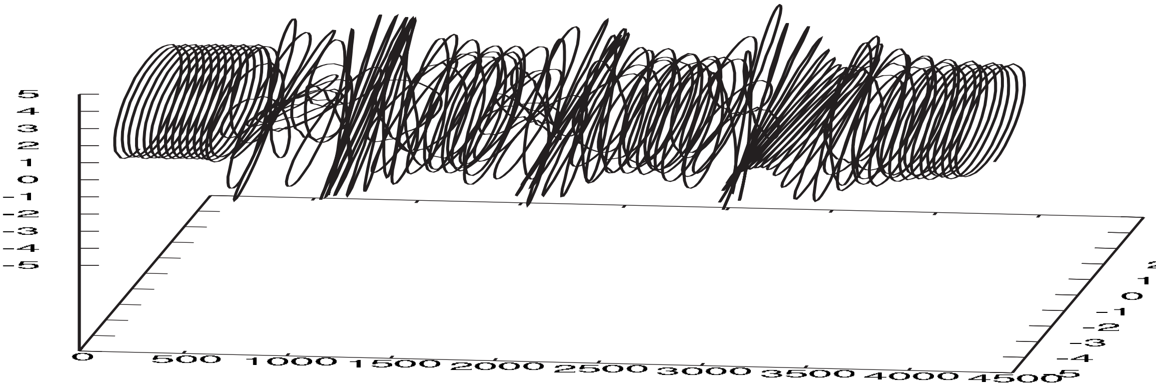

FIG. 20. Simple perspective plot of the 3D filament curve obtained for $\alpha=2.25$, $\beta=0$, $\gamma-1/8$ $(2\pi/128)=$, $L_x\times L_y\times L_z=128\times128\times4096$, $t=30\ 000$. In this disordered state, different regions can be distinguished (see text and following figure).

Moreover, the spatiotemporal diagrams in Fig. 22 clearly show the symmetry breaking between the different solutions.

From an examination of the radius in Fig. 22 we see that localized holes with zero radius are no longer observed; instead there are many regions with large rms, characteristic of flat helices and zigzag solutions. It is again useful to focus on local link density as a relevant variable in order to identify which "local state" appears as a function of this quantity. Figure 21 shows the local average of the local link density and the pitch. As in the $\gamma=0$ case, we observe regions where the local link density is no longer equal to the total link density. From a careful examination, one can even notice that regions with opposite link density are shifted to the right relative to regions where the pitch changes sign (i.e., ahead of the wave propagating to the right on spatiotemporal diagram in Fig. 22).

For $\alpha=2.05$, $\beta=0$, and $\gamma=1/8$ $(2\pi/128)$, which is close to the parameters used above, only one branch is unstable and the instability of the straight filament saturates, leading to regular helices. We carried out a 3D simulation in this regime, allowing the system to reach a stable, regular helix. Then, switching $\alpha$ back to 2.25, we observed that the regular helix solution is indeed unstable and subsequent evolution lead to a disordered state very similar that obtained starting from a straight filament (not shown). In addition, we have been able to generate an helix with the opposite twist and the

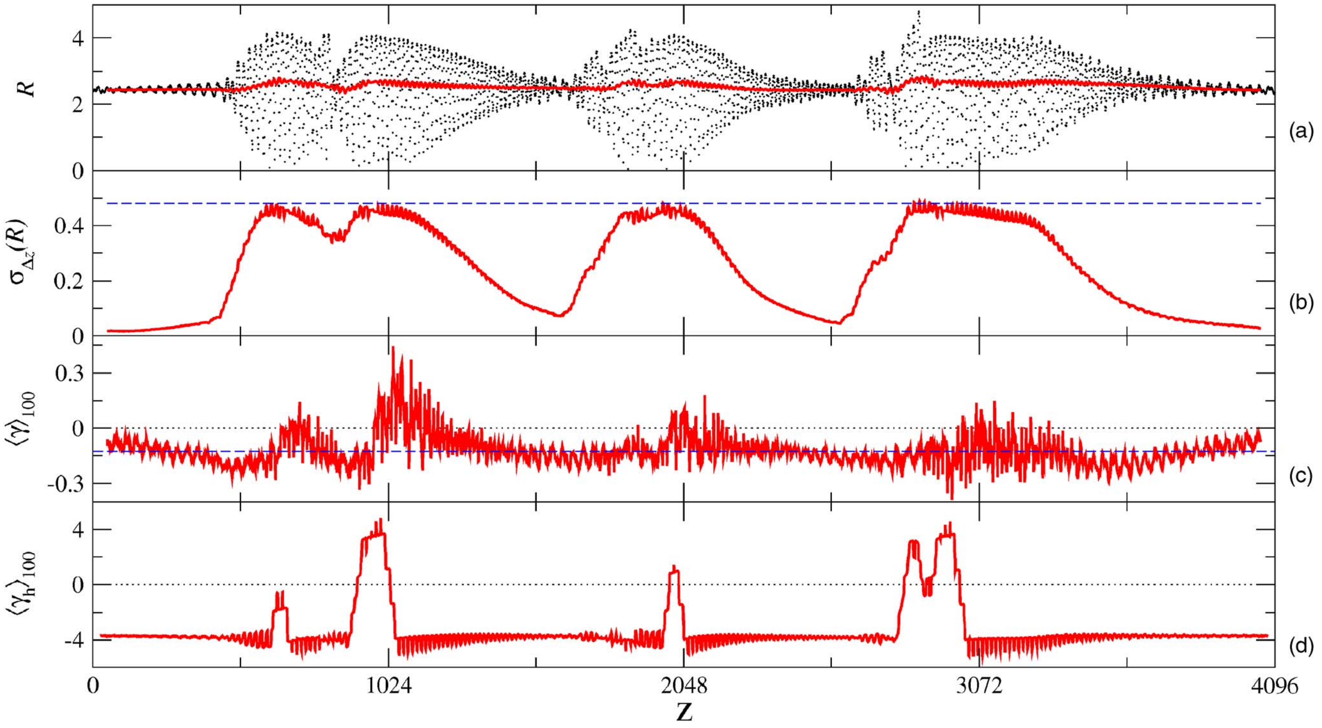

FIG. 21. (Color online) Analysis of the filament presented in Fig. 20. From top to bottom: (a) radius $R(z)$ (black dots) and locally averaged radius $\langle R(z)\rangle_{\Delta z}$ (red solid line, $\Delta z=100$). (b) Normalized rms radius $\sigma_{\Delta z}(R)/\langle R(z,t)\rangle_{\Delta z}$ calculated over $\Delta z$. The dashed line is at $\pi/(2\sqrt{2})\simeq0.48$, the value for a flat zigzag. (c) Locally averaged link density (dotted line at the mean level). (d) Locally averaged pitch.

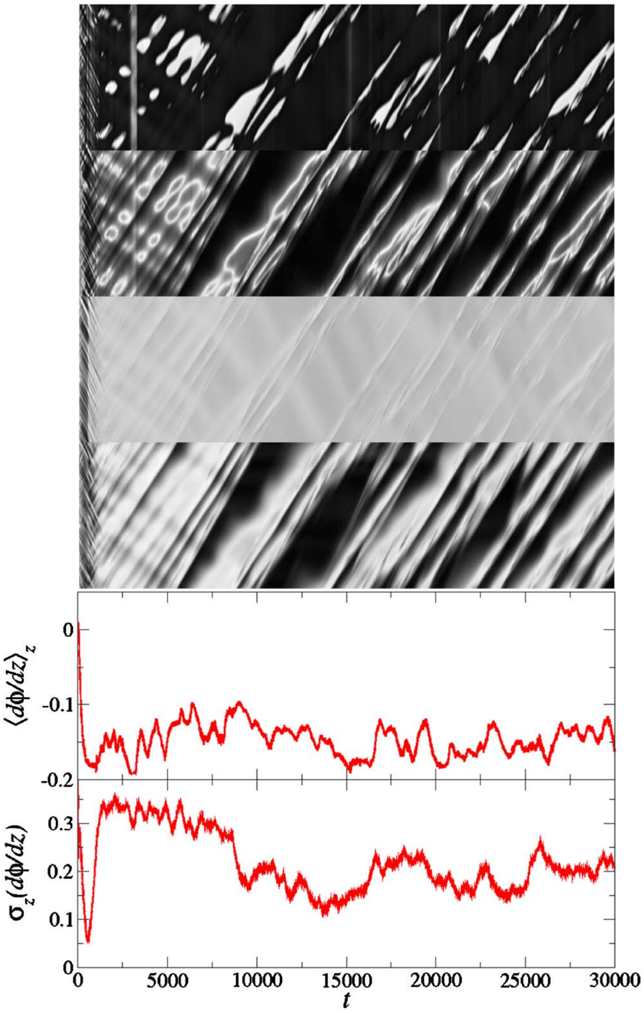

FIG. 22. (Color online) Time-evolution of various quantities during the run leading to the solution shown in Fig. 20. (Top four panels) Spatiotemporal diagrams (time is running from left to right) showing $\langle d\phi/dz(z,t)\rangle_{\Delta z}$, $\sigma_{\Delta_z}(d\phi/dz)$, $\langle R(z,t)\rangle_{\Delta z}$, and $\sigma_{\Delta z}(R)$ ($\Delta z=100$). A linear gray scale is used between instantaneous min (black) and max (white) values. (Bottom time series) $\langle d\phi/dz\rangle_z$ and $\sigma_z(d\phi/dz)$. Parameters: $\alpha=2.25$, $\beta=0$, $\gamma=-1/8$ $(2\pi/128)$, $L_x\times L_y\times L_z=128\times128\times4096$, $t=1-30\,000$.

same link density by inverting the previously obtained solution under the transformation $z\to-z$ and adding twice the link density as the phase twist. Again, we observed the instability of this initial condition, but the long time evolution did not clearly show that the final state is exactly the same. Large fluctuations observed in the average values suggest that the difference may be due to finite size effects. To sum up, we observed the instability of all initial conditions composed of "pure" local states with constant link density, and they all lead to the appearance of at least one, and perhaps two disordered states.

## V. FURTHER INSTABILITIES: SUPERHELICAL MODES

In this section, we investigate the instabilities of the stable helix solutions found when the spectrum of the straight filament solution possesses one unstable branch. The following structures can thus be seen as emerging from the secondary instability of the straight filament.

### A. Regular superhelices

As the twist density increases, (stable) helical filaments undergo further bifurcations to more complex coiled forms. A secondary supercritical Hopf bifurcation leads to a supercoiled structure described earlier.[16] The complete characterization of this supercoiling transition requires large simulation domains and careful treatment of the boundary conditions. We have performed extensive simulations of this bifurcation on large 3D cylindrical domains ($\rho=64$, $L_z=1024-2048$) using radial outflow boundary conditions and periodic boundary conditions along $z$.

#### *1. Linear regime*

The appearance of this new attractor is associated with the instability of the helix solution. There is no simple symmetry which can be used to derive a 2D equivalent equation but one can use the 2D equations to create an initial state for the 3D simulation which is as close as possible to the helix solution. One can see in Fig. 23 (middle and bottom) the destabilization of the 3D helix with $\gamma=88$ $(2\pi/2048)$, and $\gamma_h=105$ $(2\pi/2048)$. This figure also shows a spatiotemporal representation of the function $\Phi(z,t)$ defined as follows:

$$\Phi(z,t)=0 \quad \text{if } \partial\phi/\partial z<0, \qquad\qquad (18)$$
$$\Phi(z,t)=\phi(z,t) \quad \text{otherwise},$$

where $\phi(z,t)$ can be determined from the equations,

$$x_f(z,t)-\langle x_f\rangle_z(t)=R(z,t)\cos[\phi(z,t)],$$

$$y_f(z,t)-\langle y_f\rangle_z(t)=R(z,t)\sin[\phi(z,t)].$$

This function allows one to see wavelengths associated with the helix (small loops) and the superhelix mode (large loops) at the same time.

Returning to the linear regime, one can extract the real part of the eigenvalue of the most unstable mode. This was done by fitting the function $\langle R\rangle_z(t)$ to the form $R_h+Cst\ 10^{\lambda t}$ for $t\in[t_1,t_2]$. We used $t_1=200$ as a lower bound for the interpolation value assuring that the initial condition generated from the 2D solution has relaxed to a realistic 3D solution. Then the upper bound was fixed such that

$$\frac{\langle R\rangle_z(t_2)-\langle R\rangle_z(t_1)}{\langle R\rangle_z(t_1)}\simeq 0.1\ll 1. \qquad (19)$$

This ensures that the system is still in the linear regime, independent of the value of $\langle R\rangle_z(t_1)$. The inset of Fig. 23 shows the results of this procedure applied to $\langle R\rangle_z(t)$. The final result is presented in Fig. 24, where $\lambda$ versus $\gamma$, keeping the other parameters constant, is shown. It leads to the estimate $\gamma\simeq5\pm0.3$ $(2\pi/128)$ for the position of the threshold.

#### *2. Nonlinear regime*

The wavelength of the superhelical mode appearing in the early stages of the evolution is smaller than that observed in the asymptotic state (Fig. 23). To investigate the nonlinear selection of wavelengths, we performed a simulation with the same parameter values but starting from a straight filament (Fig. 25). One can observe in this case that the wave-

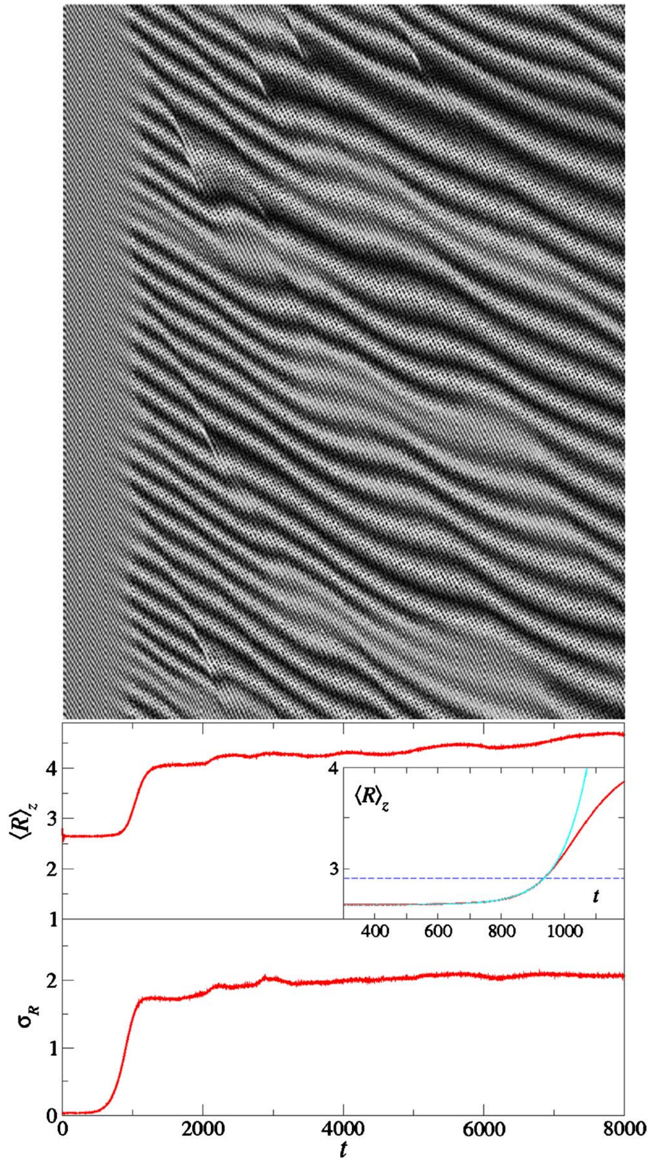

FIG. 23. (Color online) Spatiotemporal representation of $\Phi(z,t)$ (top), mean radius $\langle R\rangle_z$ (middle), and its rms $\sigma_R$ (bottom) showing the destabilization of the helix solution ($\gamma_h=1052\pi/2048$ and $\langle R\rangle_z=R_h\simeq 2.65$) for $\alpha=1$, $\beta=-0.5$, $\gamma=882\pi/2048$. Time is running from left to right. The cylindrical lattice size is $\rho=64$ (half of the diameter) and $L_z=2048$. The asymptotic wavelength is about twice that of the superhelical mode appearing in the saturation (or nonlinear) regime ($T\simeq 8000$). (Inset) Linear stage associated with the exponential growth of $\sigma_R$ and $\langle R\rangle_z-R_h$. The dashed line delimits the domain corresponding to the linear regime following the criteria defined in Eq. (18), $t_2\sim 950$. The thin line is the result of the interpolation described in the text.

length which emerges is the same throughout the saturation regime. The behavior seen starting from a helix can be viewed as an intermediate step needed to transform a helix into a superhelix. We also noticed that moving closer to the threshold the destabilization of the helical solution always leads to a transient state with a smaller wavelength.

The time needed to reach the asymptotic state (for instance, characterized by the average radius and its rms) is very long compared to the time that the system spends in the linear regime (Fig. 26). Consequently, one can study only a few cases to characterize the second instability (Fig. 27). As

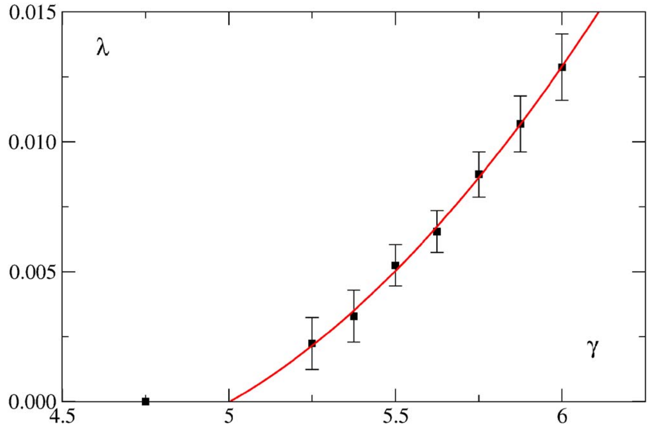

FIG. 24. (Color online) Real part of the eigenvalue of the most unstable mode of the helix solution vs $\gamma$ (in $2\pi/128$ units). Parameter values: $\alpha=1$, $\beta=-0.5$, 3D simulation with $\rho=64$, $Lz=2048$, and $dx=1$. The pitch of the helix used for the initial condition corresponds to the most unstable mode of a straight filament. Extrapolating these values gives an estimate of the threshold of the second instability around $\gamma\simeq 5\pm 0.3$ $(2\pi/128)$.

discussed in Ref. 16, we are faced with a secondary Hopf bifurcation even if the nonlinear stage appears to be more complicated.

## B. Localized superhelical loops

Increasing even further the link per unit length, one may observe more complex solutions comprising localized superhelical regions and long helical segments. These complex structures can emerge spontaneously starting from a straight filament (Fig. 28), and coexist with the stable superhelical solution: decreasing the link per unit length, one observes their persistence (Figs. 29 and 30).

The identification of localized helical and superhelical segments suggests that we can characterize the different pieces of the filament in terms of a link density. Although the writhe is a global quantity, we can split the double integral in Eq. (5), leading to the following definition of a link "density:"

$$d\gamma(s)=\tau(s)+\frac{d\phi}{ds}+\frac{1}{4\pi}\oint\frac{[\mathbf{t}(t)\times\mathbf{t}(s)]\cdot[\mathbf{X}(t)-\mathbf{X}(s)]}{|\mathbf{X}\ (t)-\mathbf{X}(s)]|^3}dt. \qquad (20)$$

The link density computed in this way for the complex filament displayed in Fig. 29 is shown in Fig. 31, along with the helix to superhelix bifurcation threshold value. One can see that the localized region where the link density exceeds the threshold value corresponds to the superhelical segment of the filament curve.

Crudely, the local link value within a superhelical segment is approximately constant. This leads one to speculate that the number of such objects per unit length must vary like $1/(\gamma-\gamma_c')$, where $\gamma_c'$ is the secondary bifurcation threshold. It then follows that the average lengths of the helical segments diverge as $\gamma$ approaches $\gamma_c'$. This is confirmed by the data in Table I which shows the number of localized structures as a function of $\gamma$.

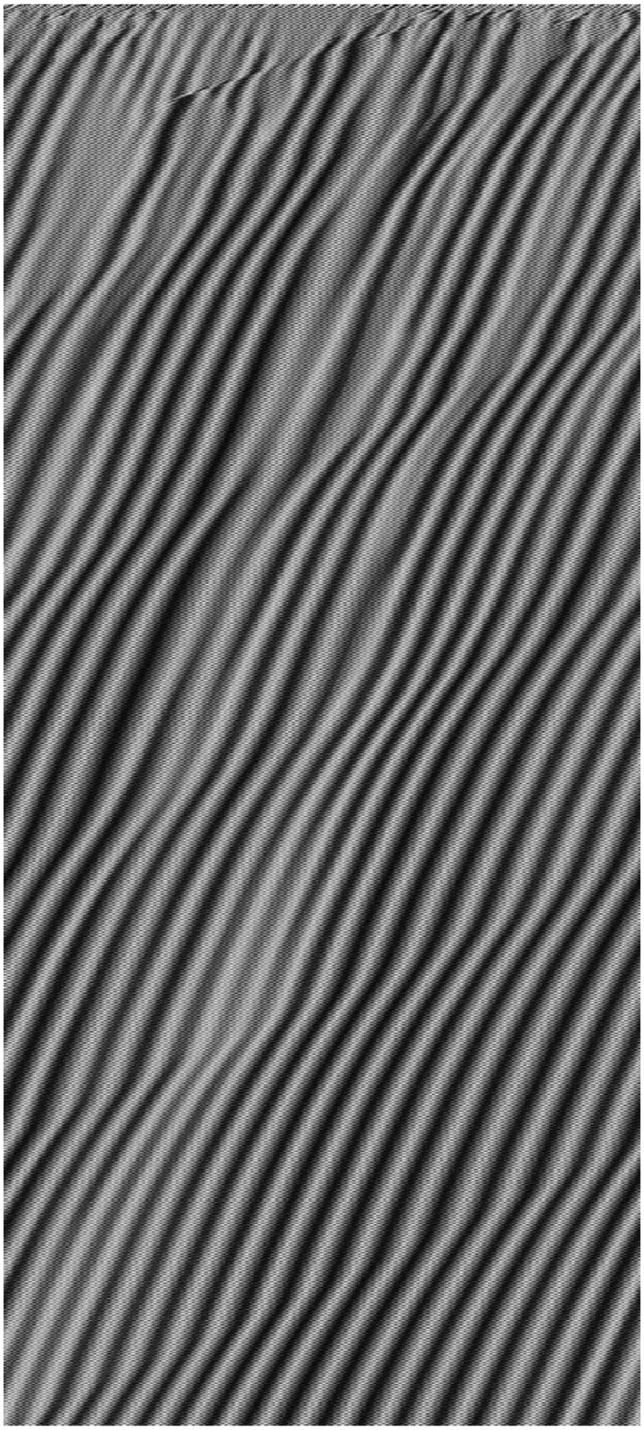

FIG. 25. Spatiotemporal representation of $\Phi(z,t)$ for the same parameter values as Fig. 23 but starting for a straight filament. Time runs downward from 0 to 28 800 (notice that this simulation is 3.6 times longer than that in Fig. 23). The wavelength of the superhelical mode is the same at short and long times. The small modulation propagating through the system is characteristic of a weak finite size effect.

Figure 31 shows that the link density of localized super helices is about $8(2\pi/128)$ and $10(2\pi/128)$. It would be interesting to increase the link density up to and above this value, but in this region of the parameter space, simulations are more difficult to carry out.

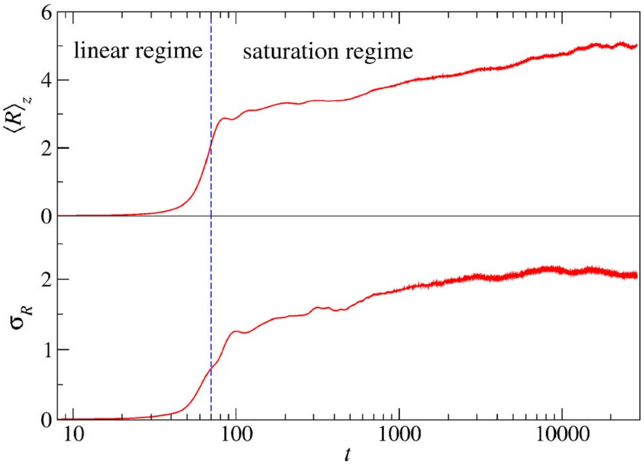

FIG. 26. (Color online) $\langle R\rangle_z$ and $\sigma_R$ vs time for the same simulation as in Fig. 25. One can see that the saturation regime is long compared to the linear regime and requires very long simulation times for its characterization.

## VI. CONCLUSION AND DISCUSSION

To summarize, we have studied the structure and dynamics of the vortex filaments that form the cores of scroll waves in the three-dimensional complex Ginzburg–Landau equation, focusing on the role that twist plays in determining the bifurcation structure in various regions of the $(\alpha,\beta)$ parameter space.

As the twist or link density $\gamma$ increases (for $\alpha$ and $\beta$ values at which the two-dimensional spiral solution in stable), initially straight filaments first undergo a Hopf bifurcation to helices. Using an equivalent 2D equation assuming helical symmetry, we have been able to carefully study this bifurcation, revealing the existence, near the $\alpha=\beta$ line for large-enough $\gamma$ values, of a region where this instability is unbounded. Furthermore, our detailed analysis has shown that saturation, when it occurs, leads to regular helices when the linear spectrum of the instability possesses only one unstable branch. When two unstable branches are present (either by symmetry when $\gamma=0$ or far enough from the stability

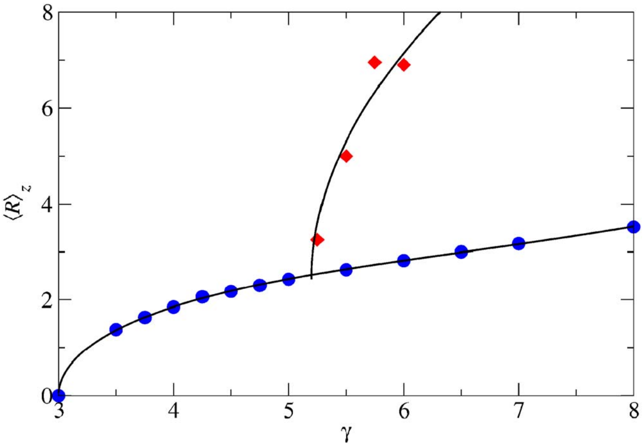

FIG. 27. (Color online) Average radius vs $\gamma$ for $\alpha=1$, $\beta=-0.5$. The lower curve (plain circles) corresponds to the helical solution, and the upper curve (plain diamonds) to the superhelical solution.

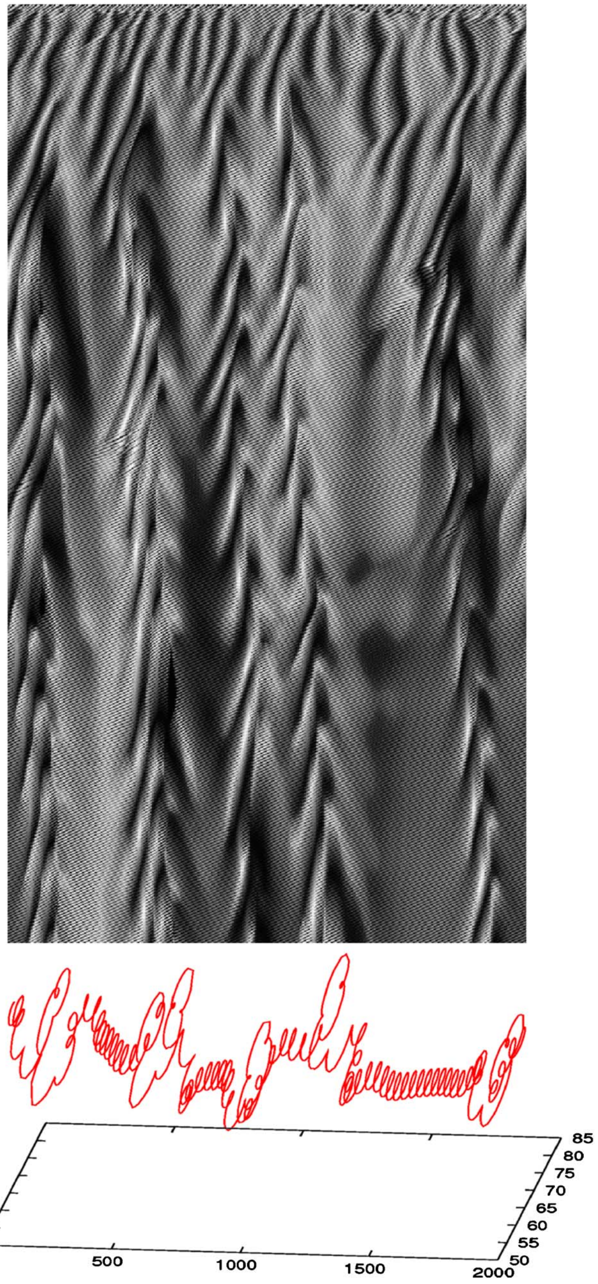

FIG. 28. (Color online) Spatiotemporal representation of $\Phi(z,t)$ for $\alpha=1$, $\beta=-0.5$, and $\gamma=6$ $(2\pi/128)$ starting from a straight filament. Time runs downward from 0 to 20 000. The lattice size is $128\times128\times2048$. After a short transient, where the super helical mode appears, one observes the nucleation of five localized structures separated by large uniform segments.

boundary when $\gamma\neq0$), no regular structures are observed in large systems. On the other hand, we showed the existence of spatiotemporally disordered regimes where rather regular helical and zigzag regions compete in a way reminiscent of spatiotemporal intermittency.

We have also shown that the regular helix solution undergoes a secondary Hopf bifurcation when $\gamma$ increases further, leading supercritically to regular supercoiled filaments. We also found indications that these superhelices are themselves subcritically unstable to—and thus may coexist with—configurations where a few localized superloops separate otherwise regular helical regions.

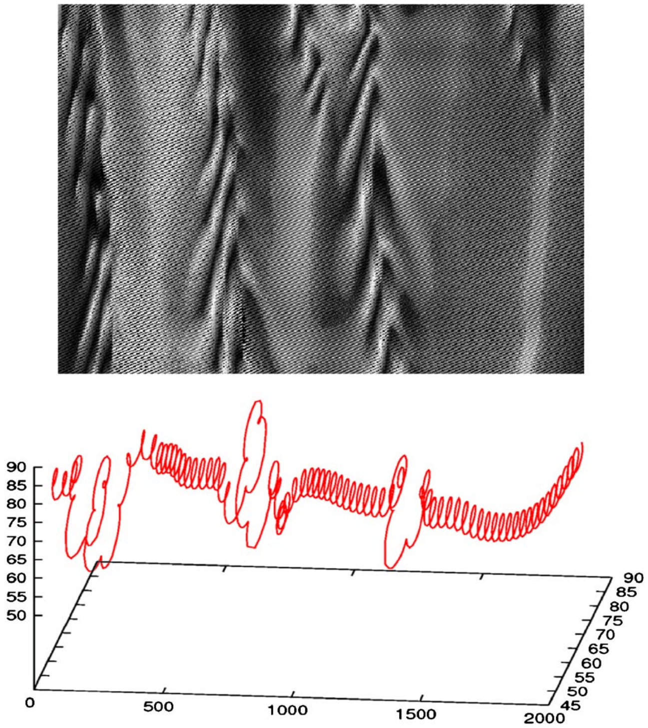

FIG. 29. (Color online) Spatiotemporal representation of $\Phi(z,t)$ and filament curve in the final state for $\alpha=1$, $\beta=-0.5$ and $\gamma=5.75$ $(2\pi/128)$ starting from the final state shown in Fig. 28. (The link number has been changed by varying the grid size.) Time runs downward from 0 to 7600. After a short transient, two of the localized objects disappear leading to larger helical segments.

Throughout the paper, we have characterized the structures observed via topological quantities suitable for twisted ribbons. We have in particular noticed that the pitch of the simple helices, $\gamma_h$, is usually close to $ks$ the wavenumber of the transverse spiral waves. Ribbon twist may thus be considered "passive," although the role of the length scale introduced by the core size needs to be studied in more detail, especially near the $\alpha=\beta$ line where this scale diverges. Interestingly, the primary Hopf bifurcation leading to helices is accompanied by a linear variation of topological quantities (such as writhe) with the imposed twist. This is reminiscent of the behavior of elastica, although here some elastic "energy" cannot be readily defined. At any rate, the limits of such an analogy are clearly manifested by the analysis of the large-scale spatiotemporally intermittent regimes observed; there, the different regular regions each seem to take their "preferred" local link density, in apparent disregard of the fixed, imposed, global link.

Many of the above statements and results require further work. It is clear, though, that further progress will require important computing power and thus will only be achievable in the future. Beyond the needed clarifications for simple oscillatory media described by the CGLE, our results need to be confronted to similar studies performed in the cases where the gauge invariance is lost either because of some external forcing (often used to control spatiotemporal dynamics) or some intrinsic local chaos (such as in Rössler oscillators), or even because the system is in fact excitable.

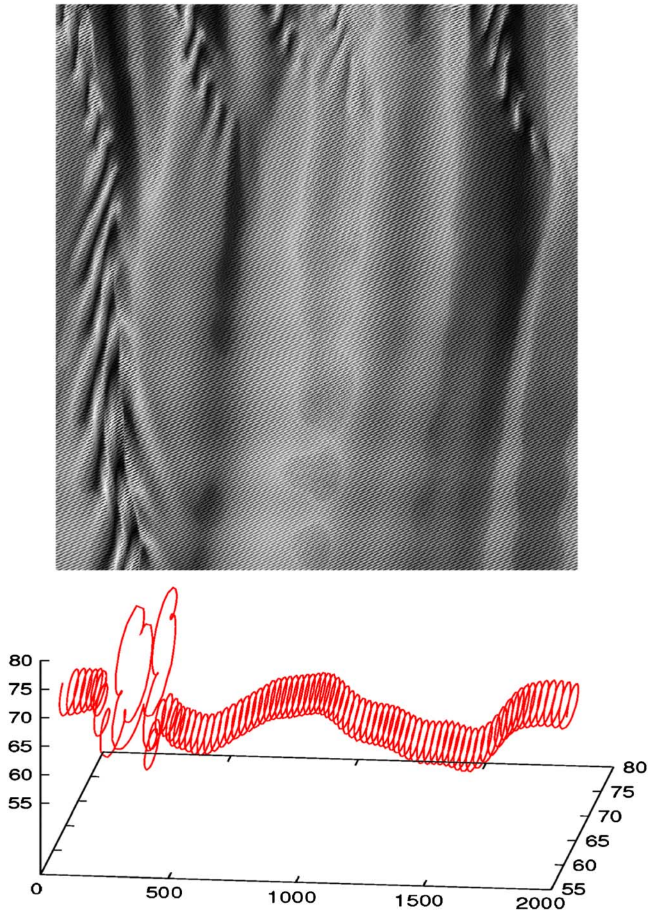

FIG. 30. (Color online) Same figure as Fig. 29 but for $\gamma=5.5(2\pi/128)$. Time runs downward from 0 to 12 000. In the final state only one localized structure remains.

TABLE I. Summary of the different runs leading to superhelical loops for $\alpha=1$, $\beta=-0.5$ in a domain of size $128\times128\times2048$. Runs #2 and #3 used the final state of run #1 as an initial condition. Finally, # *objects* is the number of localized superhelical loops still observed after a long time.

| # | $\gamma$ $(2\pi/128)$ | $\Delta t$ | $\langle R\rangle_z$ | $\sigma_R$ | $R_{\max}$ | # *objects* |
|---|---|---|---|---|---|---|
| 1 | 6 | 20 000 | 9 | 5 | 25 | 5 |
| 2 | 5.75 | 7600 | 7.4 | 4.5 | 20 | 3 |
| 3 | 5.5 | 12 000 | 4.2 | 2.5 | 17 | 1 |

A noted earlier, experimental techniques are becoming available to visualize scroll wave filaments in chemical systems, such as, the Belousov–Zhabotinsky reaction, and in biological systems, such as the heart. The investigations of the varied and sometimes complex filament structures presented in this paper will hopefully stimulate further experimental studies in this area.

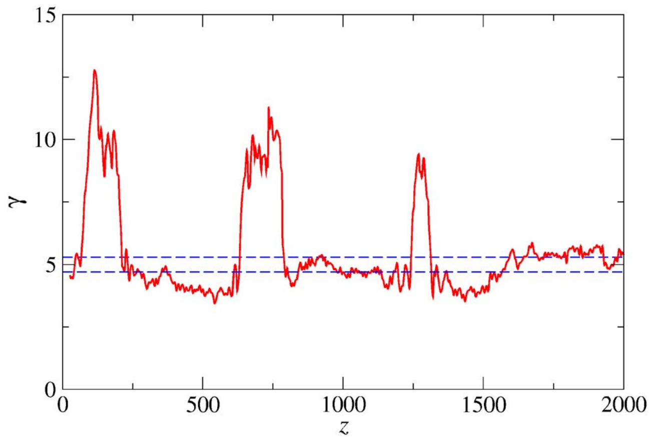

FIG. 31. (Color online) Local link density $\gamma(z)$ vs $z$ for the final state shown in Fig. 29. The upper and lower dashed lines bound the secondary instability threshold $\gamma=5\pm0.3$ $(2\pi/128)$. This shows that localized structures "concentrate" the twist in a small region of the filament such that the link density is below the secondary bifurcation threshold.

## ACKNOWLEDGMENTS

The research of R.K. was supported in part by a grant from the Natural Sciences and Engineering Research Council of Canada.

## APPENDIX A: RADIAL OUTFLOW BOUNDARY CONDITIONS

The choice of the least-interfering boundary conditions is crucial when reliable simulations free from finite-size effects are desired. Most of the configurations studied in this work are such that, far from the localized object of interest, almost-cylindrical waves are emitted.

The use of no-flux (Neumann) boundary conditions introduces fictitious mirror objects and thus the boundary may play an active role in determining the dynamics.[1] Periodic boundary conditions have similar consequences since the system must then be viewed as an array of interacting objects. Moreover, in this case, usually undesired constraints are present, e.g., the total link number must be zero. In both cases we have observed that the boundaries have a rather long-range influence on the dynamics, for instance, in selecting a significantly different pitch $\lambda_h$ for the helical filaments. As a consequence, 3D simulations free from finite-size effects are very costly if one uses no-flux or periodic boundary conditions.

This difficulty already arises in the one-dimensional case, e.g., when studying the Nozaki–Bekki holes which, asymptotically ($x\to\pm\infty$), emit plane waves. In Ref. 55, true "outflow" boundary conditions were implemented by *assuming* that propagating waves exit the system, which is the case if the boundaries are sufficiently far from the core of the amplitude hole. Letting $x_b$ be the position of the boundary, a second-order discretization scheme,

$$A(x_b,t) = A(r_b - dx,t)^2/A(x_b - 2dx,t),$$

was used, which gave excellent results, in particular when studying the sensitive issue of the linear stability of the hole solutions.

Most configurations studied here are axisymmetric with respect to the $z$ axis, as are the domains of integration. Both for the 3D and 2D equivalent cases, we assumed further that the local wavevector (or phase gradient) of the outgoing waves is oriented along a radial direction with respect to the symmetry axis. This is again a good approximation if the walls of the box are far enough from the central vortex filament. With $r$ the radial coordinate, we have

$$A(r_b,\theta,t) = A(r_b - dr,\theta,t)^2/A(r_b - 2dr,\theta,t),$$

for all $\theta$ and $t$.

For the special axisymmetric grid used to simulate the 2D equivalent equation (12), this is readily implemented. However, when a regular square lattice is used as a grid together with a circular or cylindrical domain of integration, the use of Cartesian coordinates complicates the computation. Knowing a point on the boundary, one has to interpolate the value of the complex field to points shifted in the radial direction. This interpolation can be done with varying amounts of precision and numerical tests showed that a second-order approximation is needed to obtain good results.

On each $(x,y)$ plane of a 3D cylinder, or in the plane of a 2D disk, one seeks the value $B(x_0,y_0)$ knowing the values of $B$ on the six closest lattice points. The Taylor expansion of $B$ in the neighborhood of $(x_0,y_0)$ is simply written as

$$V_{\mathcal{N}} = MV_0, \tag{A1}$$

where

$$V_{\mathcal{N}} = \begin{bmatrix} B(x_1,y_1) \\ \vdots \\ B(x_6,y_6) \end{bmatrix},$$

$$M = \begin{pmatrix} 1 & dx_1 & dy_1 & dx_1^2/2 & dy_1^2/2 & dx_1dy_1 \\ \vdots & \vdots & \vdots & \vdots & \vdots & \vdots \\ 1 & dx_6 & dy_6 & dx_6^2/2 & dy_6^2/2 & dx_6dy_6 \end{pmatrix},$$

and

$$V_0 = \begin{bmatrix} B(x_0,y_0) \\ B_x(x_0,y_0) \\ B_y(x_0,y_0) \\ B_{x^2}(x_0,y_0) \\ B_{y^2}(x_0,y_0) \\ B_{xy}(x_0,y_0) \end{bmatrix}.$$

The corrections are $\mathcal{O}(dx^3)$. One then has to solve a set of six linear equations. This was done using the $LU$ decomposition method. The most important part of the calculation is done in the initialization part of the code, where the coefficients of the decomposition are saved, and these are used throughout the simulation.

## APPENDIX B: DEFECT POSITION INTERPOLATION

The position of the defect can be defined by the crossing point (in 2D, or in a plane transverse to the filament in 3D) of a $\mathcal{R}(A)=0$ and a $\mathcal{I}(A)=0$ curve. We have developed a fast algorithm for this purpose which locates the precise position of the defect using interpolation. We have used two different estimates for the position of the defect:

- The first estimate is based on the Taylor expansion of the complex field close to coordinate singularity. We seek the point $(\delta x,\delta y)$ where the complex field is zero,

$$A(\delta x,\delta y) = 0 + i0 = A(0,0) + \delta x\partial_x A(0,0) + \delta y\partial_y A(0,0) + \mathcal{O}(\delta^2).$$

  Knowing the partial derivatives at (0,0) and neglecting second order terms, one must solve a set of two linear equations.
- The second estimate was used in the case of the polar grid on which the equivalent 2D equation (12) was simulated, when the defect is still very close to the center of the grid. It uses the symmetry of the modulus of the complex field close the defect position. Since the modulus grows linearly as a function of the distance to the defect, the value of the complex field close to the defect will be minimum along the $x$ or $y$ directions at the corresponding $x$ or $y$ component of the defect position. Using polynomial approximations to the dependence of the modulus one may estimate the defect location.

Linear dependence of the modulus implies that the square of the modulus should be well approximated by a second-order polynomial. Then the coordinate $\delta x$ is given by

$$\delta x = \frac{-B_x}{2C_x},$$

where

$$(x_1,y_1) = -(\delta r,0),$$

$$(x_2,y_2) = (0,0),$$

$$(x_3,y_3) = (\delta r,0),$$

$$B_x = -A(x_1,y_1)\frac{x_2+x_3}{(x_1-x_2)(x_1-x_3)} - A(x_2,y_2)\frac{x_1+x_3}{(x_2-x_1)(x_2-x_3)} - A(x_3,y_3)\frac{x_1+x_2}{(x_3-x_1)(x_3-x_2)},$$

$$C_x = \frac{A(x_1,y_1)}{(x_1-x_2)(x_1-x_3)} + \frac{A(x_2,y_2)}{(x_2-x_1)(x_2-x_3)} + \frac{A(x_3,y_3)}{(x_3-x_1)(x_3-x_2)}.$$

These two methods have been used for each determination of the defect position and we have verified that the relative difference between the two estimates is less than 10%.

## APPENDIX C: SIMULATION OF THE 2D EQUATION

Here, we present an outline of some features of the code written to simulate Eq. (12).

### 1. Temporal integration

A variable time step Euler scheme was used for the temporal integration. Comparisons with other schemes such as second and fourth order Runge–Kutta schemes were made and no significant improvement of stability properties was noted. To increase the order of the temporal scheme and obtain consistent results with variations of the grid size or parameters, the following variable time step algorithm was implemented.

Suppose $A(t)$ is known and an estimate of $A(t+dt)$ with a relative error smaller than $\epsilon$ is desired. The error is simply given by the distance $d$ between the exact $A$ and the approximate solution $B$,

$$d(A,B)=\frac{1}{N_p}\sum_{k=1}^{N_p}|A_k-B_k|,$$

where the sum over $k$ is over the points of the lattice. In practice, because of the inhomogeneities in the point distribution of the polar grid (see below), the maximum distance over all circular "layers" was used.

Two estimates of $A$ are obtained using the Euler scheme and two different time steps:

$$B(t+dt)=A(t)+dt\partial_t A(t),$$

$$C(t+dt)=A(t)+\frac{dt}{2}\partial_t\left[A(t)+\frac{dt}{2}\partial_t A(t)\right],$$

$$A(t+dt)=B(t+dt)-\frac{dt^2}{2}\partial_{t^2}A(t)+\mathcal{O}(dt^3),$$

$$A(t+dt)=C(t+dt)-\frac{dt^2}{4}\partial_{t^2}A(t)+\mathcal{O}(dt^3).$$

The distance between $B$ and $C$ is about the same as between $A$ and $B$ or $A$ and $C$. One can impose the condition that the distance between $B$ and $C$ must never be larger than a predetermined amount $\epsilon$. If the distance between $B$ and $C$ is too large, then this solution is not accepted and the time step is decreased. Taking into account first order nature of the scheme the new time step $dt$ is given by

$$dt_{\text{new}}=0.9dt_{\text{old}}\sqrt{\frac{\epsilon}{d(C,B)}}.$$

The 0.9 factor suppresses the contributions of higher order terms. If the distance is less than $\epsilon$, the solution is accepted but the time step is changed using the same formula under the assumption that it could be too small $[d(B,C)\ll\epsilon]$. Finally, these solutions can be used to obtain more accurate estimates of $A(t+dt)=2C(t+dt)-B(t+dt)+\mathcal{O}(dt^3)$.

### 2. Spatial derivatives

The main difficulties stem from the treatment of the spatial derivatives. We have used a polar coordinate representation of Eq. (12). The partial derivatives with respect to $\theta$ were carried out using a Fourier decomposition. Because of the nontrivial form of boundary condition (see Appendix A), a high-order finite-difference scheme was adopted for the derivatives with respect to $r$ (in contrast to a spectral decomposition),

$$\frac{\partial A}{\partial r}(r,\theta)=\{8[A(r+dr,\theta)-A(r-dr,\theta)]-[A(r+2dr,\theta)-A(r-2dr,\theta)]\}/(12dr)+\mathcal{O}(dr^4),$$

$$\frac{\partial^2 A}{\partial r^2}(r,\theta)=\{16[A(r+dr,\theta)+A(r-dr,\theta)]-[A(r+2dr,\theta)+A(r-2dr,\theta)]-30A(r,\theta)\}/(12dr^2)+\mathcal{O}(dr^4).$$

Consequently the spatial derivatives are approximated by a third-order scheme except close to the coordinate singularity where the term $1/r\partial_r A$ is of second order.

We have used Fourier decomposition to extrapolate the values of the terms $A(r\pm dr,\theta)$ when they are not defined on the lattice (cf. next subsection).

### 3. Point distribution and numerical stability analysis

The polar coordinate grid uses a variable lattice step in the angular direction. Below we describe how we determined the optimal number of points on each layer of a given radius.

As previously observed by Winfree,[17] the main difficulties with integration of a 2D reduction of the 3D problem stem from numerical instabilities which are induced by the second order derivative with respect to $\theta$. Here we present a scheme for overcoming these difficulties. For simplicity one can reduce the stability analysis to that for the equation,

$$\frac{\partial B}{\partial t}=\left(\frac{1}{r^2}+\gamma_h^2\right)\frac{\partial^2 B}{\partial\theta^2}.$$

For $r$ constant, this equation reduces to the one-dimensional diffusion equation. Using an explicit Euler scheme for the temporal integration and lowest order finite difference the following solution is obtained:

$$B(r,\theta_j,t_{n+1})=B(r,\theta_j,t_n)+\frac{\Delta t}{\Delta\theta^2}\left(\frac{1}{r^2}+\gamma_h^2\right),$$

$$[B(r,\theta_{j+1},t_n)+B(r,\theta_{j-1},t_n)-2B(r,\theta_j,t_n)].$$

One may then study the evolution of a small perturbation in discrete Fourier space $\delta B_{n,j}=\delta\tilde{B}_{n,k}\exp(ikj)$ with $k\in\{0,2\pi/N_p,\ldots,2\pi(N_p-1)/N_p\}$. One finds

$$\delta\tilde{B}_{n+1,k}=\xi(k,\Delta t,\Delta\theta)\delta\tilde{B}_{n,k},$$

with

$$\xi(k,\Delta t,\Delta x)=1-2\frac{\Delta t}{\Delta\theta^2}\left(\frac{1}{r^2}+\gamma_h^2\right)[1-\cos(k)].$$

The numerical scheme is stable if for given $\Delta t$ and $\Delta\theta$, $|\xi|<1$, $\forall k$. This is true if

TABLE II. Summary of the results of the 2D and 3D simulations for $\alpha=1.7$, $\beta=0$, $\gamma=4\pi/128$, and $\gamma_h=8\pi/128$, with radial outflow boundary conditions. The 3D system size parameters are $L_x=L_y=128/dx$ and $L_z=64/dx$. The small size in the $z$ direction places constraints on the appearance of the expected unstable mode. The 2D system radius is $n_r=45/dr$.

| | $dr,dx$ | $\lambda$ | $R$ |
|---|---|---|---|
| 3D | 0.5 | 0.0127 | 2.56 |
| 2D | 0.5 | 0.0120 | 2.50 |
| 3D | 1 | 0.0151 | 2.70 |
| 2D | 1 | 0.0131 | 2.55 |

$$\Delta t < \frac{(r\Delta\theta)^2}{2(1+r^2\gamma_h^2)},$$

which implies that the stability condition is imposed by the maximum value of $r$ if $r\Delta\theta \simeq Cst$. Note that for $\gamma_h=0$, this condition reduces to the standard result, $\Delta t < \Delta x^2/2$.

To resolve this problem we have introduced a radially dependent $\Delta\theta$, such that $\Delta\theta(r,\gamma_h) \propto \sqrt{1/r^2+\gamma_h^2}$. In addition, we have imposed the condition that the number of points in each layer is a power of 2 to obtain an efficient estimate of Fourier coefficients using fast Fourier transform methods.

### 4. Comparison of 2D and 3D simulations

We now present a comparison of the 2D and 3D simulations to show that they are in accord. The values $\gamma=4\pi/128$, $\gamma_h=8\pi/128$, were chosen since they correspond to 3D simulations for boxes of height $L_z=64$. In such boxes, an initial twist density $\gamma=4\pi/128$ gives rise to a helix with $\gamma_h=8\pi/128$. The saturated radii are comparable, and the 2D results are less sensitive to the variation of the grid size (see summary in Table II). It is interesting to consider the dependence of $\lambda$ on $dr$, the spacing used in the radial dimension, for the 2D simulations. The numerical scheme which is used is mainly of third order (see Appendix C). The correction arising from the finite grid size does indeed vary as $dr^4$ and one can easily extrapolate the results to the limit $dr \to 0$ (see Fig. 32). The result for $dr=0.5$ is already very close to the asymptotic value (0.012 00 instead of 0.011 95). In the following, we use $dr=0.5$ for all the 2D simulations, except close to the thresholds where simulations with $dr=0.25$ were performed.

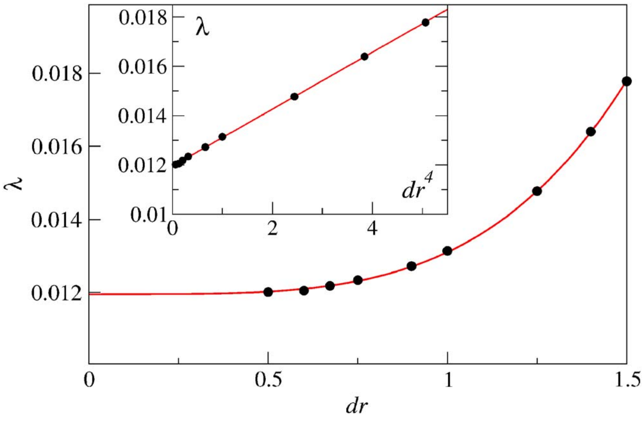

FIG. 32. (Color online) $\lambda$ vs $dr$ (grid size in radial direction) for the 2D equivalent equation. The straight line is the polynomial interpolation $\lambda(dr)=0.011\,95+0.001\,15\,dr^4$. Parameter values: $\alpha=1.7$, $\beta=0$, $\gamma=4\pi/128$, $\gamma_h=8\pi/128$.

[1] *Chemical Waves and Patterns*, edited by R. Kapral and K. Showalter (Kluwer, Dordrecht, 1994).

[2] M. C. Cross and P. C. Hohenberg, Rev. Mod. Phys. **65**, 851 (1993).

[3] A. Goldbeter, *Biochemical Oscillations and Cellular Rhythms* (Cambridge University Press, Cambridge, 1996); A. T. Winfree, *When Time Breaks Down* (Princeton University Press, Princeton, 1987).

[4] Y. Kuramoto, *Chemical Oscillations, Waves and Turbulence* (Springer-Verlag, Berlin, 1984).

[5] A. C. Newell, *Envelope Equations* (American Mathematical Society, Providence, RI, 1974).

[6] I. S. Aranson and L. Kramer, Rev. Mod. Phys. **74**, 99 (2002).

[7] I. S. Aranson, L. Kramer, and A. Weber, Phys. Rev. E **47**, 3231 (1993).

[8] H. Chaté and P. Manneville, Physica A **224**, 348 (1996); P. Manneville and H. Chaté, Physica D **96**, 30 (1996); see also C. Brito, I. S. Aranson, and H. Chaté, Phys. Rev. Lett. **90**, 068301 (2003).

[9] L. G. Brunnet, H. Chaté, and P. Manneville, Physica D **78**, 141 (1994); A. Goryachev and R. Kapral, Phys. Rev. Lett. **76**, 1619 (1996); Phys. Rev. E **54**, 5469 (1996); A. Prigent, G. Grégoire, H. Chaté, O. Dauchot, and W. van Saarloos, Phys. Rev. Lett. **89**, 014501 (2002).

[10] A. Goryachev, R. Kapral, and H. Chaté, Int. J. Bifurcation Chaos Appl. Sci. Eng. **10**, 1537 (2000); A. Goryachev, H. Chaté, and R. Kapral, Phys. Rev. Lett. **80**, 873 (1998); **83**, 1878 (1999).

[11] M. Gabbay, E. Ott, and P. N. Guzdar, Phys. Rev. Lett. **78**, 2012 (1997).

[12] I. S. Aranson, L. Kramer, and A. Weber, Phys. Rev. Lett. **72**, 2316 (1994).

[13] I. S. Aranson and A. R. Bishop, Phys. Rev. Lett. **79**, 4174 (1997).

[14] I. S. Aranson, A. R. Bishop, and L. Kramer, Phys. Rev. E **57**, 5726 (1998).

[15] K. Nam, E. Ott, P. Guzdar, and M. W. Gabbay, Phys. Rev. E **58**, 2580 (1998).

[16] G. Rousseau, H. Chaté and R. Kapral, Phys. Rev. Lett. **80**, 5671 (1998).

[17] See, for instance, A. T. Winfree, SIAM Rev. **32**, 1 (1990), and references therein.

[18] A. T. Winfree, in *Chemical Waves and Patterns*, edited by R. Kapral and K. Showalter (Kluwer, Dordrecht, 1994), p. 1.

[19] H. Henry and V. Hakim, Phys. Rev. E **65**, 046235 (2002).

[20] O. Steinbock, F. Siegert, S. C. Müller, and C. J. Weijer, Proc. Natl. Acad. Sci. U.S.A. **90**, 7332 (1993).

[21] U. Storb, C. R. Neto, M. Bär, and S. C. Müller, Phys. Chem. Chem. Phys. **5**, 2344 (2003).

[22] Focus Issue on "Fibrillation in Normal Ventricular Myocardium," Chaos **8**(1) (1998).

[23] R. H. Clayton and A. V. Holden, IEEE Trans. Biomed. Eng. **51**, 28 (2004).

[24] R. H. Clayton, E. A. Zhuchkova, and A. V. Panfilov, Prog. Biophys. Mol. Biol. **90**, 378 (2006).

[25] A. V. Panfilov, Phys. Rev. E **59**, R6251 (1999).

[26] A. B. Medvinsky, A. V. Panfilov, and A. M. Pertsov, in *Self-Organization: Autowaves and Structures Far From Equilibrium*, edited by V. I. Krinsky (Springer-Verlag, New York, 1984), p. 195.

[27] W. Jahnke, C. Henze, and A. T. Winfree, Nature (London) **336**, 662 (1988).

[28] P. K. Brazhnik, V. A. Davydov, V. S. Zykov, and A. S. Mikhailov, Sov. Phys. JETP **66**, 984 (1987).

[29] A. T. Winfree, Science **266**, 1003 (1994).

[30] V. N. Biktashev, A. V. Holden, and H. Zhang, Philos. Trans. R. Soc. London, Ser. A **347**, 611 (1994).

[31] V. N. Biktashev, Int. J. Bifurcation Chaos Appl. Sci. Eng. **8**, 677 (1998).

[32] S. Alonso, F. Sagués, and A. S. Mikhailov, Science **299**, 1722 (2003).

[33] S. Alonso, R. Kähler, A. S. Mikhailov, and F. Sagués, Phys. Rev. E **70**, 056201 (2004).

[34] M. A. Bray and J. P. Wikswo, IEEE Trans. Biomed. Eng. **49**, 1086 (2002).

[35] R. Zaritski, S. F. Mironov, and A. M. Pertsov, Phys. Rev. Lett. **92**, 168302 (2004).

[36] F. H. Fenton, E. M. Cherry, H. M. Hastings, and S. J. Evans, Chaos **12**, 852 (2002).

[37] A. Rusakov, A. B. Medvinsky, and A. V. Panfilov, Phys. Rev. E **72**, 022902 (2005).

[38] T. Bánsági and O. Steinbock, Phys. Rev. E **76**, 045202 (2007).

[39] A. V. Panfilov and A. N. Rukenko, Physica D **28**, 215 (1987).

[40] F. Chavez, R. Kapral, and L. Glass, Chaos **11**, 757 (2001).

[41] A. V. Panfilov and A. T. Winfree, Physica D **17**, 323 (1985).

[42] P. J. Nandapurkar and A. T. Winfree, Physica D **29**, 69 (1987).

[43] A. M. Pertsov, R. R. Aliev, and V. I. Krinsky, Nature (London) **345**, 419 (1990).

[44] C. Henze, E. Lugosi, and A. T. Winfree, Can. J. Phys. **68**, 683 (1990).

[45] J. P. Keener, Physica D **31**, 269 (1988).

[46] H. Chaté, Nonlinearity **7**, 185 (1994); B. I. Shraiman *et al.*, Physica D **57**, 241 (1992).

[47] P. Hagan, SIAM J. Appl. Math. **42**, 762 (1982).

[48] M. Tabor and I. Klapper, Nonlinear Sci. Today **4**, 7 (1994); **4**, 12 (1994).

[49] J. H. White, Am. J. Math. **91**, 693 (1969).

[50] A reduction of the 3D dynamics to 2D with the assumption that $\gamma_p=0$ (a restriction not valid here) was considered by Winfree (Ref. 17), but the results of numerical simulations were not reported due to the numerical difficulties encountered in the simulation of the equivalent 2D equation.

[51] A. Goriely and M. Tabor, Proc. R. Soc. London, Ser. A **454**, 3183 (1980).

[52] J. Lega, Physica D **152**, 269 (2001).

[53] M. van Hecke, C. Storm, and W. van Saarloos, Physica D **134**, 1 (1999).

[54] M. Golubitsky and M. Roberts, J. Differ. Equations **69**, 216 (1987).

[55] H. Chaté and P. Manneville, Phys. Lett. A **171**, 183 (1992); J. Burguete, H. Chaté, F. Daviaud, and N. Mukolobwiez Phys. Rev. Lett. **82**, 3252 (1999).